



Published in final edited form as:

Nature. 2016 April 7; 532(7597): 58–63. doi:10.1038/nature17427.

Thalamic reticular impairment underlies attention deficit in *Ptchd1*^{Y/-} mice

Michael F. Wells^{1,2,*}, Ralf D. Wimmer^{3,4,*}, L. Ian Schmitt^{3,4}, Guoping Feng^{2,5,†}, and Michael M. Halassa^{3,4,6,7}

¹Department of Neurobiology, Duke University Medical Center, Durham, NC 27710, USA

²McGovern Institute for Brain Research, Department of Brain and Cognitive Sciences, Massachusetts Institute of Technology, Cambridge, MA 02139, USA

³Neuroscience Institute, New York University Langone Medical Center, New York, NY 10016, USA

⁴Department of Neuroscience & Physiology, New York University Langone Medical Center, New York, NY 10016, USA

⁵Stanley Center for Psychiatric Research, Broad Institute of MIT and Harvard, Cambridge, MA 02142, USA

⁶Department of Psychiatry, New York University Langone Medical Center, New York, NY 10016, USA

⁷Center for Neural Science, New York University, New York, NY 1003, USA

Abstract

Developmental disabilities, including attention-deficit hyperactivity disorder (ADHD), intellectual disability (ID), and autism spectrum disorders (ASD), affect 1 in 6 children in the United States. Recently, *PTCHD1* (Patched-domain containing protein 1) gene mutations have been found in ~1% of patients with ID and ASD. *PTCHD1* deletion patients show symptoms of ADHD, sleep disruption, hypotonia, aggression, ASD, and ID. Although *PTCHD1* is likely critical for normal development, the connection between its deletion and the ensuing behavioral defects is poorly understood. Here, we report that during early postnatal development, mouse *Ptchd1* is selectively expressed in the thalamic reticular nucleus (TRN), a group of GABAergic neurons that regulate thalamo-cortical transmission, sleep rhythms, and attention. *Ptchd1* deletion attenuates TRN activity by reducing calcium-dependent potassium currents (SK). Restricted TRN deletion of *Ptchd1* leads to attention deficits and hyperactivity, both of which are rescued by pharmacological

Users may view, print, copy, and download text and data-mine the content in such documents, for the purposes of academic research, subject always to the full Conditions of use: http://www.nature.com/authors/editorial_policies/license.html#terms

†Corresponding author: Guoping Feng, ; Email: fengg@mit.edu

*These authors contributed equally to this work

Author Contributions:

MFW and GF conceived the genetic studies and designed associated experiments, while RDW and MMH conceived the physiologic studies and designed associated experiments. All authors designed the behavioral studies. MFW and RDW collected the data. MFW, RDW, and LIS analyzed the data. MFW, RDW, MMH, and GF interpreted the results. MFW, MMH, GF wrote the paper with input from RDW.

The authors declare no competing financial interests.

augmentation of SK channels. Global *Ptchd1* deletion recapitulates learning impairment, hyper-aggression, and motor defects, all of which are insensitive to SK pharmacological targeting and not found in the TRN-restricted deletion mouse. This study maps clinically-relevant behavioral phenotypes onto TRN dysfunction in a human disease model, while also identifying molecular and circuit targets for intervention.

Recent genetic studies have revealed significant overlaps of risk genes across seemingly distinct neurodevelopmental and psychiatric disorders including autism spectrum disorder (ASD), attention-deficit hyperactivity disorder (ADHD), schizophrenia, and intellectual disability (ID) [1–4]. Such shared genetic architectures could potentially explain the overlap of behavioral abnormalities across these diagnostic categories, but because of the difficulty in mapping circuitry mechanisms of behavior, understanding how diverse genetic lesions converge onto behavior-relevant circuit dysfunction has been limited.

Here we focused on *PTCHD1*, a gene that is mutated in about 1% of all patients with ASD and ID [5–10]. Comprehensive clinical analysis of *PTCHD1* deletion patients identified a variable, non-syndromic neurodevelopmental disorder with symptoms ranging from attention deficit, hyperactivity, sleep abnormality, hypotonia, and learning disability [11]. We found that *Ptchd1* was selectively expressed in the thalamic reticular nucleus (TRN) of the mouse in early development and continued to be enriched in this structure throughout adult life. The TRN is critical for thalamo-cortical transmission [12–15], generation of sleep rhythms [12, 16–18], sensorimotor processing [19, 20], and attention [13, 21], and its perturbation could result in deficits in these domains. By generating a *Ptchd1* knockout (KO) mouse, we recapitulated many of these human symptoms. Critically, we mapped ADHD-like behaviors onto TRN circuit dysfunction via two independent methods. First, by deleting *Ptchd1* selectively from the TRN, we replicated the attention deficit and hyperactivity behaviors, but not other disease-related phenotypes found in the full KO. Second, pharmacological rescue of TRN biophysical dysfunction selectively rescued these ADHD-related behaviors in the *Ptchd1* KO. These findings constitute the first evidence for a “leaky thalamus” in a neurodevelopmental disorder, where irrelevant inputs that are normally suppressed become highly distracting. Most importantly, we identified the TRN and its SK channels as circuit and molecular targets for intervention.

Altered TRN neuronal biophysics

The X-linked *Ptchd1* gene is predicted to encode a twelve-pass transmembrane protein with a sterol-sensing domain (SSD) [5], prompting its classification as a member of the Patched family and speculation that it may function as a Sonic hedgehog receptor [22–24]. Prenatally, *Ptchd1* expression is found in the developing cerebellum and diencephalon [www.eurexpress.org; Ref Seq XM_142262]. We found *Ptchd1* mRNA to be confined to the TRN at birth, and by P15 onwards, to be expressed in the striatum, cortex, and cerebellum (Fig. 1a–b, Ext. Data Fig. 1, Supplemental Table 1). Interestingly, Patched family members *Ptchd2* and *Ptchd3* show no TRN expression [Allen Brain Atlas; Exp 77620810 & Exp 71891731, respectively]. Thus, *Ptchd1* may play a unique role in the TRN.

To understand how *Ptchd1* deletion might contribute to neurodevelopmental disorders, we generated a conditional allele of *Ptchd1* by targeting Exon 2 (Ext. Data Fig. 2a). This exon encodes 3 out of the 12 transmembrane domains including a significant portion of the SSD. Loss of this exon is predicted to generate a prematurely terminated non-functional protein (Ext. Data Fig. 2b). *In situ* hybridization, genotype PCR, and cDNA transcript analyses confirmed successful excision of Exon 2 (Ext. Data Fig. 2c–e; For source data, see Supplemental Figure 1). Because *Ptchd1* is X-linked and patients are almost exclusively males, we used hemizygous male mice (*Ptchd1*^{Y⁻}; referred to as *Ptchd1* KO) for this study. *Ptchd1* KO mice were viable with normal body weight allowing for direct genetic modeling of this human condition.

Given the enriched expression of *Ptchd1* in the TRN, we focused our initial investigation on this structure in *Ptchd1* KO mice. The TRN is a group of GABAergic neurons that provide the major source of inhibition to thalamic relay nuclei, and are thought to regulate cortical rhythms, sleep, and attention [21, 25, 26]. To begin investigating possible physiological changes in the KO mice, we exploited a well-known characteristic of TRN neurons. Depending on their resting membrane potential, these neurons fire in two distinct modes upon receiving synaptic input [27]. At depolarized membrane potential, they fire tonic Na⁺ spikes. When hyperpolarized, they generate repetitive “low-threshold” Ca²⁺ transients crowned by high-frequency Na⁺ spikes known as bursts [26, 28–30]. Whole-cell patch-clamp recordings of TRN neurons revealed a significant decrease in repetitive bursting in KO mice compared to wild-type (WT) controls (Fig. 1c–d). These changes were not the result of altered KO TRN neuron resting membrane potential, input resistance, or escape from hyperpolarization (Fig. 1d, inset).

Because repetitive bursting is known to depend on interactions between T-type Ca²⁺ and small conductance calcium-activated (SK) K⁺ channels [26], we asked which of these two conductances were primarily impaired in the KO. Under voltage clamp, we found T currents to be intact but SK currents to be reduced by 50% in the KO (Fig. 1e–h). We took note that SK channels are sensitive to resting state intracellular Ca²⁺ ([Ca²⁺]_i) [26, 31] and measured this concentration using the ratiometric Ca²⁺ indicator Fura-2AM in TRN neurons from acute brain slices. We found a two-fold reduction of [Ca²⁺]_i in KO TRN neurons (Fig. 1i), suggesting that altered Ca²⁺ homeostasis may underlie SK channel deficits.

Reduced TRN-generated sleep spindles

Previous studies have suggested that TRN bursting plays a role in the generation of sleep spindles [19, 28], predicting that the diminished bursting found in *Ptchd1* KO mice would lead to reduced sleep spindles. Using independently adjustable multi-electrode arrays to directly target TRN neurons for electrophysiological recordings in freely behaving animals and surface electroencephalography (Fig. 2a, Ext. Data Fig. 3a) [32], we discovered that KO TRN neurons exhibited reduced burst firing in sleep (Fig. 2b) and KO mice showed overall reduction in sleep spindle count (Fig. 2c, Ext. Data Fig. 3b–c). Further, the degree of TRN neuronal engagement in spindle events was substantially diminished in the KO (Ext. Data Fig. 3d–f), supporting the link between the cellular and network phenotypes in this disorder and perhaps other human neurodevelopmental disorders [33, 34]. Importantly, consistent

with the notion that sleep spindles are a marker for sleep stability [35, 36], we found *Ptchd1* KO mice to display highly fragmented sleep (Fig. 2d–f; Supplemental Table 2).

Impaired sensory-evoked thalamic inhibition

In addition to reduced rebound bursting, insufficient K^+ -mediated hyperpolarization is expected to more generally alter TRN neuronal excitability. Most importantly, it could lead to neurons not being hyperpolarized enough for T-type Ca^{2+} channels to de-inactivate and boost excitability [24]. Therefore, despite finding T-type currents to be intact under controlled voltage clamp conditions (at $-70mV$), insufficient hyperpolarization caused by reduced SK current would render T-type channels less recruitable under physiological conditions [17], leading to reduced TRN neuronal activity and diminished overall thalamic inhibition. To test this prediction at the population level and in the intact brain, we used chloride photometry, a tool that we recently developed as a proxy for population-level GABAergic inhibition [13]. This technique utilizes FRET-based measurements of the chloride-sensor SuperClomeleon [37], a reporter composed of a cyan fluorescent protein (CFP) FRET-donor and a chloride-quenchable yellow fluorescent protein (YFP) FRET acceptor (Fig. 3a). By introducing SuperClomeleon into visual thalamic neurons (lateral geniculate nucleus, LGN; Fig. 3b) we observed visual-evoked chloride transients (Fig. 3c–d), replicating our recent findings [13]. Visual-evoked inhibitory transients were observed in both WT and *Ptchd1* KO LGN, but a quantitative comparison revealed a 25% reduction of these transients in the KO (Fig. 3e–g). Impaired inhibition was also observed in response to trains of stimuli (Fig. 3h, j). Interestingly, a small inhibitory augmentation as a result of repeated stimulation was observed in WTs and this augmentation was also significantly reduced in the KOs (Fig. 3h–i). Altogether, these findings provide direct evidence for reduced thalamic inhibition in *Ptchd1* KO mice and are consistent with impaired TRN output with ensuing deficits in sensory-related thalamic inhibition.

ADHD-like behaviors in *Ptchd1* KO mice

We have recently observed that thalamic inhibition is utilized to suppress unwanted sensory inputs during attention [12]. The observed reduction in thalamic inhibition (Fig. 3) would predict that unwanted sensory inputs may become particularly distracting for *Ptchd1* KO mice. To test this hypothesis, we trained mice on a visual detection task shown to require attentional engagement [12] (Fig. 4a). Mice initiated each trial by continuously breaking an infrared barrier for 0.5–0.7 seconds, ensuring proper head position when a visual stimulus was presented either to the right or left of the animal. Correct indication of visual stimulus location by nose-poking resulted in reward delivery. Under such conditions, *Ptchd1* KO mice performance was comparable to WTs (Fig. 4b). However, in the presence of a visual distractor during anticipation, KO mice showed impaired performance (Fig. 4c). The specific distractibility phenotype, rather than a more general failure of attentional engagement, revealed by this novel behavioral paradigm is consistent with the prediction of impaired thalamic inhibition required for distractor suppression. It is also consistent with clinical findings in patients with related neurodevelopmental disorders [38]. This impairment was not the result of general sensorimotor dysfunction given intact performance on standard sensorimotor testing (Ext. Data Fig. 4a–c).

Distractibility is often accompanied by hyperactivity in several human neurodevelopmental disorders such as ADHD [39, 40]. ADHD symptoms are frequently observed in patients with *PTCHD1* mutations [11]. Interestingly, *Ptchd1* KO mice showed a hyperactivity phenotype in the open field (Fig. 4d). Classical ADHD-related hyperactivity is predicted to respond effectively to amphetamines, as had been previously described in other mouse models of neurodevelopmental disease [41]. Surprisingly, *Ptchd1* KO hyperactivity was insensitive to amphetamine treatment (Fig. 4e–f), suggesting a unique pathophysiological origin that may be related to the approximately 30% of ADHD patients who do not respond to amphetamines [42].

In addition to attention deficits and hyperactivity, *Ptchd1* KO mice showed a variety of behavioral abnormalities. While KO mice showed intact performance on tasks requiring simple spatial learning (Ext. Data Fig. 5a–d), they exhibited significant deficits on tasks necessitating more complex associations that are believed to require integration across multiple brain structures [43]. KO mice showed fear-induced freezing deficits in contextual (Fig. 4g) and cued (Fig. 4h) fear conditioning paradigms. Impaired learning was corroborated by profound deficits on the inhibitory avoidance task (Fig. 4i). KO mice also exhibited motor defects such as gait abnormalities (Ext. Data Fig. 5e) and hypotonia (Ext. Data Fig. 5f), as well as hyper-aggression (Ext. Data Fig. 5g–h). All of these behaviors were independent of genetic background (Ext. Data Fig. 6). These behaviors are consistent with clinical findings of multi-system abnormalities in *PTCHD1* deletion patients, suggesting the major function of *PTCHD1* is evolutionarily conserved. Interestingly, while several *PTCHD1* deletion patients have been diagnosed with ASD, KO mice did not exhibit differences in repetitive grooming (Ext. Data Fig. 7a) or social interaction (Ext. Data Fig. 7b–c). This may reflect evolutionary divergence either in *PTCHD1* function or in behavioral circuits related to *PTCHD1* deficiency [44].

TRN defects underlie ADHD-like behaviors

To determine which behavioral abnormalities are caused by TRN dysfunction, we sought strategies to largely limit *Ptchd1* deletion to the TRN. To choose the appropriate Cre-driver line to breed with floxed *Ptchd1* (*Ptchd1^{+/fl}*) mice, we looked for specific TRN overlap between candidate markers and *PTCHD1* expression. Immunohistochemical co-labeling experiments of *Ptchd1-YFP^{+/-}*, a novel knock-in mouse with Yellow Fluorescent Protein (YFP) in place of *Ptchd1* Exon 1 (Ext. Data Fig. 8a), revealed significant and unique overlap between YFP and the inhibitory neuronal marker GAD67 in the TRN (Ext. Data Fig. 8b; Supplemental Table 3).

Both parvalbumin (PV) and somatostatin (SOM) are inhibitory neural markers that are widely expressed across TRN neurons [45, 46] and showed overlap with YFP limited to this region (Ext. Data Fig. 8c), suggesting that mating Cre-drivers of either PV or SOM to *Ptchd1^{+/fl}* mice would result in a *Ptchd1* deletion that is primarily confined to the TRN. Given the early postnatal expression of *PTCHD1* and SOM in the TRN (Ext. Data Fig. 9), we reasoned that the *Som-Cre* mouse would be a more suitable choice for such experiments [47]. We crossed *Ptchd1^{+/fl}* female mice to *Som-Cre* mice and generated male mice lacking *Ptchd1* in the TRN (*Som-Cre⁺:Ptchd1^{Y/fl}*), as confirmed by *in situ* hybridization (Fig. 5a).

Som-Cre⁺:Ptchd1^{Y/fl} mice displayed attention deficits (Fig. 5b) and recapitulated the hyperactivity phenotype observed in the germline KO (Fig. 5c–d), suggesting that these behaviors are explained by TRN dysfunction. *Som-Cre⁺:Ptchd1^{Y/fl}* mice showed intact learning (Fig. 5e) and did not show hypotonia or hyper-aggression (Ext. Data Fig. 10a–b), reaffirming the circuit specificity of this genetic model. Interestingly, *Som-Cre⁺:Ptchd1^{Y/fl}* mice exhibited fragmented sleep (Ext. Data Fig. 10c–e), confirming the notion that sleep abnormalities observed in the germline KO are of TRN origin, and that sleep and attention deficits can arise from common circuit dysfunction [48].

Finally, we asked whether pharmacological boosting of SK channels could rescue ADHD-like KO behaviors. Acute injection of the SK positive allosteric modulator 1-ethyl-benzimidazolone (1-EBIO) significantly mitigated impaired sensory-evoked thalamic inhibition in germline KOs with no impact on inhibitory transients in the WT mice (Fig. 6a). Consistent with these physiological effects, 1-EBIO did not impact attentional task performance in the WT mice (Fig. 6b) but substantially mitigated distractibility in the KO mice (Fig. 6c). In addition, 1-EBIO injection rescued the hyperactivity phenotype in the KOs (Fig. 6d–e). Specificity of this pharmacological approach was supported by it not impacting other abnormalities including hypotonia (Ext. Data Fig. 10f), hyper-aggression (Ext. Data Fig. 10g), and learning deficits (Fig. 6f). Together, these results further support SK channel dysfunction as a cellular mechanism for these behavioral abnormalities. Future studies examining the therapeutic benefit of SK targeting for sleep fragmentation and instability and its potential relevance to inattention would be important.

Discussion

To our knowledge, this study is the first to show that a TRN circuit deficit is central to a specific set of behavioral impairments in a human neurodevelopmental disease model. Utilizing a conditional knockout approach of *Ptchd1*, a gene whose expression is restricted to the TRN during early postnatal development, we mapped behavioral phenotypes onto their circuit substrates. We additionally discovered that modulation of SK channel function might be explored as a potential novel treatment strategy for *PTCHD1* deletion patients with attention deficits and hyperactivity. Hyperactivity of TRN origin may be the motor equivalent of sensory distractibility, which could involve dysfunctional motor TRN-thalamic circuits. Future experiments exploring inhibitory control of motor thalamus will formally test this conjecture.

While basic studies have shown the TRN to be central for attention [21, 49] and sleep spindles [16], our study directly shows how disease-relevant impaired TRN output can result in attention deficits, hyperactivity, and sleep disruption. This direct demonstration was made possible by developing SuperClomeleon photometry, a technique that can now be widely applied to disease models as a screen for impaired thalamic inhibition. It is possible that a “leaky thalamus” caused by impaired TRN function underlies attention deficits, hyperactivity, and sleep disruption across various neurodevelopmental disorders, and we expect the set of genetic, physiologic, and behavioral approaches we introduce here to facilitate such discoveries.

Methods

Ptchd1 conditional KO mice

Ptchd1 conditional knockout mice were generated by homologous recombination in R1 embryonic stem cells and implanted in C57Bl/6J blastocysts using standard procedures. The targeting vector was designed to flank Exon 2 of the *Ptchd1* gene with loxP sites and a NEO cassette. Chimaeric mice were crossed to C57Bl/6J females (Jackson Labs). Germline transmission was determined by genotyping PCR of mouse tail DNA, using primer pFW Pt1cKO Gen 1a (GGATGGTACCACCTACAATATGC) and pRV Pt1cKO Gen 3b (AAGCCAAAGAGTTTACCCTG) for the wild-type allele (187 base pairs) and the floxed allele (227 base pairs). The F1 hybrids were crossed to C57Bl/6J β -Actin Flp mice to excise the NEO cassette. The floxed mice were then backcrossed to C57Bl/6J mice for 5 generations. After the 5th generation, speed congenic genotyping PCRs were conducted to determine the approximate purity of the background. Only mice showing >95% C57Bl/6J background were used for subsequent matings. Backcrossed *Ptchd1* KO mice were then bred with C57Bl/6J β -Actin Cre mice to produce germline knockouts of the floxed allele. Genotypes were determined by PCRs using the pFW Pt1cKO Gen 1a and pRV Pt1cKO Gen 4c (GGACTTTGGAGTAAACCACC; in the NEO cassette) primers for the knockout allele (351 base pairs). For all behavioral experiments in the C57Bl/6J background, *Ptchd1*^{Y/-} (KO) and *Ptchd1*^{Y/+} (WT) males were bred with *Ptchd1*^{+/-} females. For the C57/129 mixed background behavioral experiments, 129^{+/+} males were bred with *Ptchd1*^{+/-} C57Bl/6J females and the F1 offspring were used for experiments. Animals were housed 3–5 by genotype per cage at a constant 23°C in a 12 h light/dark cycle (lights on at 07:00) with ad libitum food and water (unless otherwise noted).

Healthy age-matched male mice between 2–5 months were used for all behavioral experiments. Sample sizes were chosen based on standards in the field as well as previous experience with phenotype comparisons. All behavior experiments employed a group counterbalancing strategy to ensure that both genotypes were being tested at equal frequencies throughout the testing day. For drug studies, mice were chosen at random to be included in the vehicle-treated versus drug-treated groups. Experimenters were blind to genotype, but not group (i.e. Group A vs Group B), during data acquisition and analysis. D'Agostino and Pearson omnibus normality tests were run. When normality was violated, non-parametric tests (Wilcoxon ranksum) were used. ANOVA was used to estimate group variance where multiple comparisons were made. All data analyzed with two-tailed t-tests showed similar variances between groups. Data presented as scatterplot with mean denoted by bar, unless otherwise noted. All animal experiments were conducted according to the NIH Health Guide for Care and Use of Laboratory Animals and were approved by the Massachusetts Institute of Technology Institutional Animal Care and Use Committee.

Ptchd1-YFP mice

Ptchd1-YFP mice were generated by homologous recombination in R1 embryonic stem cells and implanted in C57Bl/6J blastocysts using standard procedures. The targeting vector replaced Exon 1 of the mouse *Ptchd1* gene with ATG-eYFP-STOP cassette and a NEO cassette. Correctly-altered ES colonies were PCR screened using primers targeting the YFP

insert and long-arm PCR (LA Taq) methods. Chimaeric mice were crossed to C57Bl/6J females from Jackson Labs. Germline transmission was assessed through genotyping PCR of mouse tail DNA, using primers pFW Pt1-YFPki Gen 3a (TTACTTCCTTTTCCCCACC), pRV Pt1-YFPki Gen 3a (CCCAGGTTCTCTAGTAGATTCC), and pFW Pt1-YFPki Gen 3b (GGAGAGTGAATCTAGGTGGAG) for the wild-type allele (positive band = 190 base pairs) and the YFP positive allele (positive band = 316 base pairs). The F1 hybrids were backcrossed to C57Bl/6J mice for 2 generations. Female mice containing the YFP insertion (*Ptchd1-YFP^{+/-}*) were used for all immunohistochemistry experiments.

In situ hybridization

mRNA *in situ* hybridization was performed with 20 μ m cryosections from freshly frozen P0, P15, and P35 brain tissue from male mice using a mixture of two digoxigenin (DIG)-labelled probes against mouse *Ptchd1* cDNA (GenBank Accession NM_001093750.1; Ex2 base pairs 372-1006 and Ex3 base pairs 1290-2027), except for the WT-KO comparisons, in which only Ex2 probe was used. The hybridization signal was detected using an alkaline phosphatase (AP)-conjugated anti-DIG antibody (Roche) and developed using 5-bromo-4-chloro-indolylphosphate/nitroblue tetrazolium (BCIP/NBT; Roche). Sections were imaged using an Olympus BX61 motorized fluorescent microscope.

Immunohistochemistry

Mice were perfused with ice-cold 1X PBS and 4% paraformaldehyde. Brains were then fixed overnight at 4°C prior to vibratome sectioning. Fifty micron sections were washed with 1X PBS 3 \times 5 mins prior to a 1 hr room temperature incubation in blocking solution (5% normal goat serum, 2% BSA, 0.2% Triton X-100 in 1X PBS). Sections were then incubated overnight at 4°C in primary antibody solution: Rabbit anti-GFP (Invitrogen A11122; 1:1000), Chicken anti-GFP (Abcam 13970; 1:1000) Mouse anti-GAD67 (Millipore 5406; 1:1000), Rabbit anti-Somatostatin (Peninsula Labs T4102; 1:1000), and Mouse anti-NeuN (Millipore MAB377; 1:1000). Following the 3 \times 20 mins wash in 1X PBS, tissue was incubated for 4 hrs at room temperature in second antibody solution: Goat anti-Rabbit Alexa 488 (LT A-11034; 1:1000), Goat anti-Rabbit Alexa 555 (LT A-21428; 1:1000), Goat anti-Mouse Alexa 488 (LT A-11001; 1:1000), Goat anti-Mouse Alexa 555 (LT A-21422; 1:1000), and Goat anti-Chicken Alexa 488 (LT A-11039; 1:1000). Sections were once again washed 3 \times 20 mins in 1X PBS prior to mounting onto glass slides using Fluoro-Gel. Images were taken with an Olympus Fluoview 1000 confocal microscope. YFP co-labeling was quantified using ImageJ. Images were converted to 8-bit files and automatically background subtracted and thresholded. The resulting images were converted to a mask and then the processes “fill holes” and “watershed” were implemented. The processed images were then analyzed using the “analyze particles” feature with the squared size set to “200-Infinity” and the show feature set to “outlines.” This end product of this procedure was an image containing enumerated cell skeletons. Skeleton images from the green and red channels were merged and overlapping skeletons were counted as a co-labeling event.

Slice electrophysiology

Freshly prepared brain slices from P21-P28 male mice were superfused with oxygenated ACSF (in mM: 125 NaCl, 25 NaHCO₃, 25 glucose, 2.5 KCl, 1.25 NAH₂PO₄, 1.2 MgCl₂, 2

CaCl₂, 1.7 ascorbic acid) and recorded at 30–34°C. Patch pipettes (2.5–4 MΩ) contained the following intracellular solution in mM: 140 KMeSO₄, 10KCl, 10 HEPES, 0.1 EGTA, 4Mg-ATP, 0.2 Na-GTP, 10 phosphocreatine, (285 mOsm, pH 7.2). For rebound burst characterization, cells were held in current clamp at potentials ranging from –85 to –25 mV through constant current injection. Rebound bursting was determined following a 600 ms, –0.5 nA current step. Events crossing 2 standard deviations of the baseline noise were considered bursts. To determine T and SK currents, responses to different hyperpolarizing steps (500 ms, ranging from –110 to –60 mV) were recorded in voltage clamp configuration. T currents were isolated through application of the SK channel blocker apamin (100 nM) while SK currents were estimated by digital subtraction of the isolated T current from control currents without apamin in slices from 4–5 mice per genotype. Cells where the input resistance changed > 15% during the recording were excluded from the analysis.

In vivo TRN recordings

Hyperdrives containing 12 individually adjustable microdrives loaded with 1–2 stereotrodes were built as previously described [37]. Mice were anesthetized with 1% isoflurane and mounted on a stereotaxic frame. A 3 × 2.5 mm craniotomy (center coordinate M–L: 2.5 mm, A–P: –1.3 mm) was drilled and the hyperdrive was implanted at a 15° angle relative to midline. At time of implantation, stereotrodes were lowered <500 microns into the brain. Three stainless steel screws (one located prefrontal and two cerebellar) served as EEG electrodes and ground and anchored together with two additional fixation screws the hyperdrive to the skull. After recovery, mice were connected to a custom made 32-channel preamplifier headstage (Neuralynx, Bozeman, MT) and data was acquired using a Neuralynx Digilynx recording system. Stereotrode signals were amplified, filtered between 0.1 Hz and 9 kHz and digitized at approximately 30 kHz. Spikes were manually clustered using the MClust toolbox for MATLAB, and bursts were identified as at least two spikes with inter-spike interval > 10 ms which were preceded by > 70 ms of silence. Spindle detection was performed as previously described [12]. The EEG signal was filtered within the spindle frequency band (9–15 Hz) and the Hilbert transform (MATLAB function “hilbert”) was computed. The envelope of the signal (1 s smoothing) was used as a basis for spindle detection. A threshold of one standard deviation (SD) was applied and each threshold crossing, with parameters of > 0.5 s and < 3 s, were initially included. These events were subsequently visually inspected before being included in the analysis. To assess consistency in the phase locking of individual TRN neurons with spindles, we used spike phase synchrony analysis between unit firing and spindle band (9–15 Hz) filtered component of the LFP (Ext. Data Fig. 3d–f). For each TRN unit we first constructed a spike-phase histogram of firing rates relative to alpha. Units were considered significantly phase locked if the distribution of spike phases significantly differed from a uniform distribution based on Rayleigh’s test for circular uniformity (cut-off, $p < 0.05$). To quantify the degree of phase-locking, the Pearson’s correlation coefficient between spike counts and phase angle was computed for each unit. Analysis was performed in MATLAB using the circular statistics toolbox.

Sleep analysis

Sleep-related immobility was used to measure sleep bout duration in mice (C57: 9 WT and 10 KO; Som-Cre: 10 WT and 10 KO), a technique that has previously been shown to correlate ($r = 0.94$) with EEG recordings [50]. We used BIOBSERVE Behavioral Sequencer boxes (BIOBSERVE; Bonn, Germany) that utilize Piezo sensors and video recordings to automatically score 23 different movements/behaviors, including immobility (Sequencer label “STILL”). The lighting inside the boxes were set to 5–10 lux, which mimicked home cage light intensity in the MIT animal holding facility. Mice were placed into a custom-made transparent plastic cylinder (diameter: 16 cm x height: 16 cm) containing home cage bedding in order to reduce the arena parameters and facilitate sleep. At 7AM, mice were placed in the behavioral sequencers and given 1 hour to acclimate. After the acclimation period, behavior was automatically scored for 6 hours (8AM–2PM). Data was manually curated to identify bouts of sleep, which were defined as at least 40 seconds of immobility [50] that is not interrupted by more than 2 seconds of upper body movements (Sequencer labels “HEAD”, “FACE”, “NOSE”, “CHEEK”, “BACK”, “ORIENT_LOOK”, “ORIENT_SNIFF”) or by 4 or more seconds of general body movements (Sequencer labels “PAW”, “LEG”, “TUMMY”, etc.). These bout parameters were confirmed by two observers viewing raw video during pilot tests. Behavioral recordings and analysis were conducted by a genotype-blind experimenter. Given the 40 second minimum required to be classified as a bout, median data and cumulative probability were used to compare genotypes. Kolmogorov-Smirnov and the Wilcoxon ranksum tests were used for statistical analysis. All individual data points are plotted with crossbar denoting median.

Fibre-photometry-based optical chloride measurements

Mice (6 WT and 6 KO) were injected with 400 nl of AAV-hSyn-SuperClomeleon into the LGN (from Bregma A–P: –2 mm, M–L: –2.1 mm, D–V: –2.5 mm) and chronically implanted with optical fibres (400 μm , Doric lenses, Canada) targeted directly above LGN (D–V: 2.1 mm). Following at least two weeks of virus expression, FRET-based measurement of visual evoked $[\text{Cl}^-]_i$ responses was performed as previously described [13]. Briefly, CFP excitation was achieved through a fibre-coupled LED (Thorlabs, Newton, New Jersey) light source, filtered using a 434 nm clean-up filter (MF434-17 Thorlabs, Newton, New Jersey) and light was delivered to the LGN via a 600 μm , 0.48 NA optic patch cord (Fig. 2g). SuperClomeleon CFP and YFP emissions were separated using a single-edge beam splitter (FF511-Di01, Semrock, Rochester, New York) and collected using two femtowatt silicon photoreceiver (Newport, Irvine, California). Signal was digitized and recorded using a TDT signal acquisition system (Tucker-Davis Technologies, Alachua, Florida). Visual stimulation consisted of a 50 ms LED light pulses delivered to the eye contralateral to the recorded LGN. Normalized delta fluorescence (df/F) was calculated for evoked responses relative to the baseline fluorescence level before each event (1-s window) and smoothed with a convolution filter (50 ms half-width). The minimum signal within a 500 ms window following stimulation was considered the peak response. For pharmacological SK channel enhancement, mice were injected with 25 mg/kg 1-EBIO following 30 min of baseline recordings. Maximal drug effects were estimated from evoked responses recorded between 30 min to 1 h following injection.

Visual detection task

Mice (C57: 8 WT and 9 KO from 2 independently-tested cohorts; Som-Cre: 8 WT and 8 KO from 2 independently-tested cohorts; EBIO: 7 WT-Veh, 7 WT-EBIO, 7 KO-Veh, 7 KO-EBIO) were food restricted to 85–90% of their *ad libitum* body weight and training occurred in a custom built test chamber as previously described [32]. During testing, a white noise indicated that a new trial was available, and mice had to continuously break an infrared barrier for 500–700 ms to initiate a trial. Upon successful initiation, a 50 ms visual stimulus was presented randomly either on the left or right side. Correct response at the corresponding nose-poke unit resulted in a milk reward (10 μ l evaporated milk, Nestle) that was available for 15 sec. Following an intertrial interval (ITI) of 5 sec a new trial became available. Response at the incorrect location resulted in immediate blockage of poke access and a 30 sec timeout before the next trial. To test for distractibility, in one third of the trials a 50 ms distractor appeared at the opposite location of where the stimulus would be displayed in the 200 ms time window before successful initiation. For drug treatment experiments, mice were injected with 1-EBIO (Tocris #1041; 25 mg/kg in 10% DMSO; subcutaneous injection) or vehicle 30 mins prior to testing. Wilcoxon ranksum test was used for statistical analysis. All individual data points are plotted with crossbar denoting median.

Fura-2AM Calcium imaging

Freshly prepared brain slices from P21-P28 male mice (4 WT and 5 KO) were superfused with oxygenated ACSF (in mM: 125 NaCl, 25 NaHCO₃, 25 glucose, 2.5 KCl, 1.25 NAH₂PO₄, 1.2 MgCl₂, 2 CaCl₂, 1.7 ascorbic acid) and recorded at 30–34°C. Cells (37 WT, 36 KO) were filled with Fura-2AM dye (Molecular Probes) using a Picospritzer II that applied ~10 psi for 1 min through a 1–2 M Ω glass pipette. Slices were given 1 hr to recover in ACSF prior to imaging. Individual cells were imaged using an Olympus BX61WI microscope with an attached CoolSnapF2 camera. Pixel intensity was measured using ImageJ software with whole-field background correction. Ratiometric values were converted to [Ca²⁺]_i using the following equation:

$$[Ca^{2+}]_i = K_d * (R - R_{min}) / (R_{max} - R) * S_{f2} / S_{b2}$$

where K_d refers to the Ca²⁺ dissociation constant (140 nM), R refers to the ratiometric measurement of the observed cell, R_{max} and R_{min} correspond to the ratio under conditions of saturated Ca²⁺ levels and in zero Ca²⁺, respectively. The values of S_{b2} (bound state) and S_{f2} (free Ca²⁺ state) are proportional to the fluorescence excited by 380 nm under conditions of saturated Ca²⁺ levels and in zero Ca²⁺, respectively. Unpaired t-tests were used to compare nM concentrations between the two groups. Data presented as mean \pm s.e.m.

Open Field

Locomotor activity in mice (C57: 30 WT and 31 KO from 3 independently-tested cohorts; MIX: 10 WT and 11 KO from 1 cohort; AMPH: 5 WT-Veh, 5 WT-AMPH, 6 KO-Veh, 6 KO-AMPH; EBIO: 13 WT-Veh, 13 WT-EBIO, 13 KO-Veh, and 15 KO-EBIO from 2 independently-tested cohorts; Som-Cre: 21 WT and 22 KO from 2 independently-tested cohorts) was evaluated over a 60 min period in an automated Omnitech Digiscan apparatus

(AccuScan Instruments) as previously described (Peca et al., Nature 2011). Locomotor activity was assessed as total distance travelled (m). Anxiety-like behavior was defined by number of rearings and time spent in the center as compared to time spent in the perimeter (thigmotaxis) of the open field. For drug treatment experiments, mice were placed in the open field arena for 30 minutes prior to amphetamine (3 mg/kg in saline; intraperitoneal injection), 1-EBIO (25 mg/kg in 10% DMSO; subcutaneous injection), or vehicle injections. Mice were then returned to open field arena for an additional 30–90 minutes. Two-way repeated measures ANOVA with Bonferroni post-hoc tests were used for statistical analysis. Time binned data (“distance”) presented as mean \pm s.e.m. Summated data (“total distance”) plotted as individual data points with crossbar denoting mean. One C57 KO mouse was excluded for escaping from the arena during testing.

Grooming

Young adult male mice (C57: 9 WT and 13 KO from 1 cohort; MIX: 10 WT and 12 KO from 1 cohort) were used for analysis of grooming behavior. Individually housed animals were habituated in the testing room for one hour prior to experimentation. Mice were videotaped for 2 hr under 2 lux (red light) illumination. Grooming behaviors were coded from 19:00–21:00 hr (2 hr beginning at the initiation of the dark cycle). This segment was analyzed using Noldus Observer software and the total amount of time in the 2 hr segment spent grooming was determined. A genotype-blind observer recorded all types of grooming, including incidences of face-wiping, scratching/rubbing of head and ears, and full-body grooming. Two-tailed t-tests were used for statistical analysis. All individual data points are plotted with crossbar denoting mean.

Rotarod

Motor coordination was assessed in mice (C57: 19 WT and 21 KO from 2 independently-tested cohorts; MIX: 10 WT and 10 KO from 1 cohort) using an accelerating rotarod test (Med Associates) over the course of two days. On the first day (training day) animals underwent three 5 min trials at a constant speed (16 rpm). On the second day (testing day), animals underwent three 5 min trials at accelerating speeds (4–40 rpm). For all trials, the latency to fall was determined. Animals were tested for three trials in a single day with an inter-trial interval of 10–30 min. Two-way repeated measures ANOVA with Bonferroni post-hoc tests were used for statistical analysis. Data plotted as mean \pm s.e.m. Two C57 KO mice were excluded for jumping off the rotarod during testing.

Hanging Wire

Animals (C57: 12 WT and 11 KO from 1 cohort; MIX: 10 WT and 12 KO from 1 cohort; EBIO: 6 WT-Veh, 6 WT-EBIO, 6 KO-Veh, and 6 KO-EBIO from 1 cohort; Som-Cre: 12 WT and 11 KO from 1 cohort) were suspended 40 cm above the ground from a 2mm horizontal wire. The average of three trials with an inter-trial interval of 5 mins was recorded. For drug treatment experiments, mice were injected with 1-EBIO (Tocris #1041; 25 mg/kg in 10% DMSO; subcutaneous injection) or vehicle 30 mins prior to testing. Two-tailed t-tests were used for statistical analysis. All individual data points are plotted with crossbar denoting mean.

Gait

The forepaws of animals (C57: 10 WT and 11 KO from 1 cohort) were painted green and the hindpaws were painted pink. After a two minute habituation trial, the mice were allowed to walk down a 50 cm track. The length and width of each stride were measured by an observer blind to genotype and the averages were recorded. Two-tailed t-tests were used for statistical analysis. All individual data points are plotted with crossbar denoting mean.

Hot Plate

Animals (C57: 20 WT and 21 KO from 2 independently-tested cohorts; MIX: 10 WT and 12 KO from 1 cohort) were placed onto a heating block set to 55°C surface temperature (Columbus Instruments). Latency to lick a forepaw or hindpaw was measured. The average of three trials with an inter-trial interval of 5 mins was recorded. Two-tailed t-tests were used for statistical analysis. All individual data points are plotted with crossbar denoting mean.

Acoustic startle and pre-pulse inhibition

Auditory abilities and sensory motor function in mice (C57: 20 WT and 21 KO from 2 independently-tested cohorts; MIX: 10 WT and 12 KO from 1 cohort) was measured using Hamilton Kinder Scientific Pre-pulse Startle Monitor chambers with Startle Monitor software. On the first day, mice underwent a 5 min acclimation trial in the acoustic startle boxes. On the second day, half of the mice were tested on the acoustic startle protocol while the other half was tested on the pre-pulse inhibition protocol. These protocol groups were switched on the third day. To test acoustic startle, mice are presented with pulses of various dB level without pre-pulses for approximately 30 mins. The testing session is preceded by a 5 min exposure to 65 dB background noise. Each mouse then receives a total of 92 stimuli (trials) with inter-trial intervals ranging from 7–23s presented in pseudo-random order. The stimuli include a presentation of 8 pulse-alone trials (120 dB, 40 ms pulse, 4 at the beginning and 4 at the end of the session), 77 pulse trials (7 each of 70, 75, 80, 85, 90, 95, 100, 105, 110, 115, and 120 dB, 40 ms pulse), and 7 trials each without pulse or pre-pulse presentation. To test PPI, mice were once again exposed to 65 dB background for 5 min prior to testing. Each mouse received a total of 57 stimuli (trials) with inter-trial intervals ranging from 7–23s presented in pseudorandom order. The stimuli include a presentation of 8 pulse-alone trials (120 dB, 40 ms pulse, 4 at the beginning and 4 at the end of the session), 35 pre-pulse trials (7 each of 70, 75, 80, 85 and 90 dB, 20 ms pre-pulse given 100 ms prior to a 120 dB, 40 ms pulse), and 7 trials each without pulse or pre-pulse presentation. The PPI percentage within each test session was calculated as follows: $[100 - (\text{mean Pre-pulse response} / \text{mean Pulse response}) \times 100]$. For all experiments, response to startle stimuli is measured in Newtons (N). Startle at each pulse level is averaged across trials and then across animals in a treatment group. Two-way repeated measures ANOVA with Bonferroni post-hoc tests were used for statistical analysis. Data plotted as mean \pm s.e.m.

Three-chambered social interaction assay

Littermate male mice (C57: 10 WT and 11 KO from 1 cohort; MIX: 10 WT and 12 KO from 1 cohort) were used for all tests. Age and size-matched 129 male target subjects (Stranger 1 and Stranger 2) were habituated to being placed inside wire cages for three days (20 mins/

day) before beginning of testing. Test mice were habituated to the testing room for at least 1hr before the start of behavioral tasks. The social test apparatus consisted of a transparent acrylic box with removable floor and partitions dividing the box into three chambers. The wire cages used to contain the stranger mice were cylindrical, 11 cm in height, a bottom diameter of 10.5 cm with the bars spaced 1 cm apart (Galaxy Cup, Spectrum Diversified Designs). An inverted metal can was placed on the top of the cage to prevent the test mice from climbing on the top of the wire cage. For the sociability test, the test animal was introduced to the middle chamber and left to habituate for 10 mins. Following this period, the middle chamber doors were opened and the test mouse was allowed to freely explore all three chambers for an additional 10 mins. The test mouse was then returned to the middle chamber, after which an unfamiliar mouse (Stranger 1) was introduced into a wire cage on one of the side-chambers and an empty wire cage on the other side-chamber. The dividers were then raised and the test animal was allowed to freely explore all three chambers over a 10 min session. Following the 10 min session, the mouse was returned to the middle chamber while a novel stranger mouse (Stranger 2) was inserted in the wire cage previously empty and again the test animal was left to explore for a 10 min session. The time spent by the mouse (nose-point) in close proximity (~5cm) to the wire cages was calculated using automated software (Noldus Ethovision 9). The release of the animals and relative position of social and inanimate targets was counterbalanced. However, for each individual test animal the location of Stranger 1 was maintained during Stranger 1 – E and Stranger 1 – Stranger 2 testing of the social behavior. One-way ANOVA with Bonferroni multiple comparison tests were used for statistical analysis. All individual data points are plotted with crossbar denoting mean.

Resident intruder

Animals (C57: 10 WT and 10 KO from 1 cohort; EBIO: 6 WT-Veh, 6 WT-EBIO, 6 KO-Veh, 6 KO-EBIO from 1 cohort; Som-Cre: 6 WT and 6 KO from 1 cohort) were individually housed for 2 weeks prior to testing with bedding left undisturbed for one week prior to testing. Animals were tested in a room with 10 lux lighting. On the test day, animals were habituated to the test room for 1 hour prior to testing. After acclimation, an age and weight-matched conspecific male stranger mouse was introduced to the home cage of the test animal. The subsequent interactions were videotaped for 5 minutes. All interactions were analyzed using Noldus Observer by a genotype-blind observer. Aggressive interactions were defined by instances of biting, fighting, and tail-rattling. For drug treatment experiments, mice were injected with 1-EBIO (Tocris #1041; 25 mg/kg in 10% DMSO; subcutaneous injection) or vehicle 30 mins prior to testing. Wilcoxon ranksum and Kruskal-Wallis non-parametric tests were used for statistical analysis because WT mice did not pass normality tests. All individual data points are plotted with crossbar denoting median.

Inhibitory avoidance

Animals (C57: 24 WT and 23 KO from 2 independently-tested cohorts; MIX: 10 WT and 12 KO from 1 cohort; EBIO: 7 WT-Veh, 8 WT-EBIO, 9 KO-Veh, and 10 KO-EBIO from 2 independently-tested cohorts; Som-Cre: 11 WT and 12 KO from 1 cohort) underwent one training session followed by 24hr and 48hr post-training trials. On the training day, mice were placed in the light side of the IA box (Ugo Basile) and allowed to habituate for 30 sec.

To quantify pre-shock latency and the effects of baseline locomotor activity levels on this task, the door to the dark side of the box was then opened and the latency to cross was measured. Upon entering the dark side of the box, the mice were given a 0.5mA shock for 2–4 seconds, followed by a 60 sec post-shock habituation. On the probe trials, mice were placed in the light side of the box with the door to the dark side already opened. Latency to cross was once again measured with a maximum duration of 9 mins. For drug treatment experiments, mice were injected with 1-EBIO (Tocris #1041; 25 mg/kg in 10% DMSO; subcutaneous injection) or vehicle 30 mins prior to the shock training protocol. Two-way repeated measures ANOVA with Bonferroni post-hoc tests were used for statistical analysis. All individual data points are plotted with crossbar denoting mean.

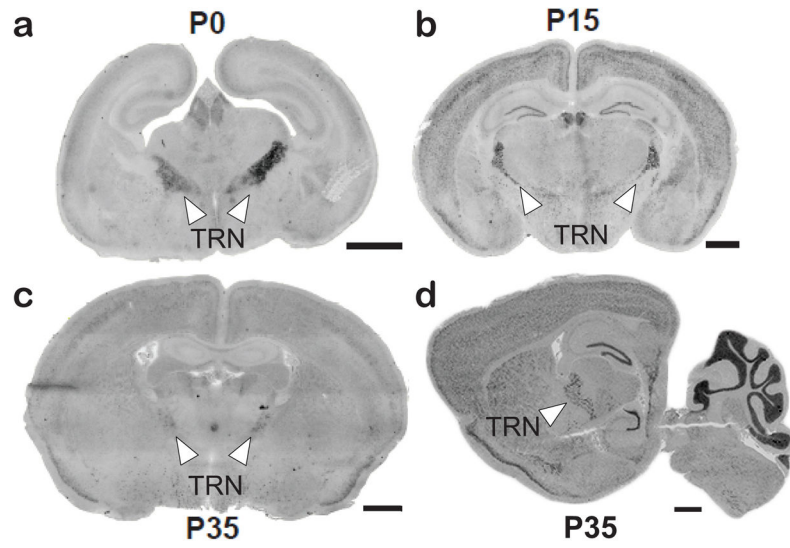
Fear conditioning

Animals (C57: 10 WT and 11 KO from 1 cohort) were tested for fear-induced freezing using Med Associates fear conditioning chambers encased in sound attenuating cubicles optimized for near infrared (NIR) video recording. The training protocol involved a 3 min habituation period in the conditioning box, followed by three rounds of a 30 sec tone + 2 sec/0.75 mA shock + 90 sec rest. The final shock was followed by a 2 min post-training habituation. The following day, mice were returned to the conditioning box and the time spent freezing was measured. Four hours after, the mice were returned to the conditioning boxes with modifications. A white triangular insert was added to change the dimensions of the box and 0.1% acetic acid was sprayed onto the base of the box in order to change the scent of the box. Once again, the time spent freezing over the course of 5 minutes was measured. Freezing was measured using Video Freeze software package analysis of NIR recordings. Two-tailed t-tests were used for statistical analysis. All individual data points are plotted with crossbar denoting mean.

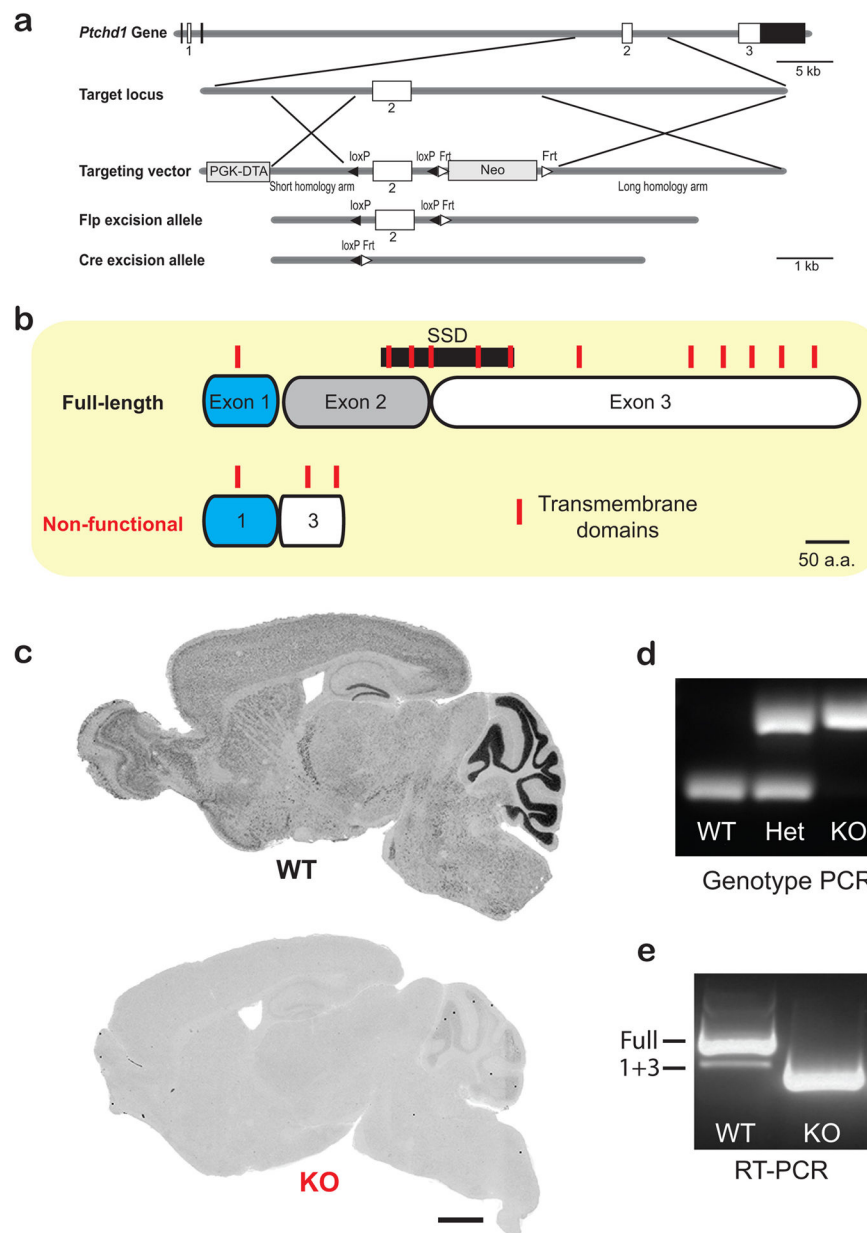
Morris water maze

Spatial learning testing in mice (C57: 10 WT and 10 KO from 1 cohort) was conducted using a testing pool that was 120 cm in diameter and a platform 8 cm in diameter. The platform was submerged 1 cm below the water surface. Pool water was maintained at 23.0 ± 0.5 °C and made opaque by mixing-in white non-toxic white paint. During training, 90 sec duration trials were used. If the animals did not find the platform within 90 sec, the experimenter guided the animal to the platform. After reaching the platform the animals were left for 15 sec on top of the platform before being removed. Trials were administered for 5–6 days with four trials per animal per day with the platform located in the NW quadrant. For two consecutive days after the training protocol, 60 sec probe trials were performed (one per day). The reversal training commenced with the platform in the SE quadrant, and proceeded as described above. The experimenter followed the animals' progress using tracking software outside of the testing room. Tracking and analysis were performed using the Noldus Ethovision software. Two-way repeated measures ANOVA with Bonferroni post-hoc tests and one-way ANOVA with Bonferroni multiple comparison tests were used for statistical analysis. All individual data points are plotted with crossbar denoting mean.

Extended Data

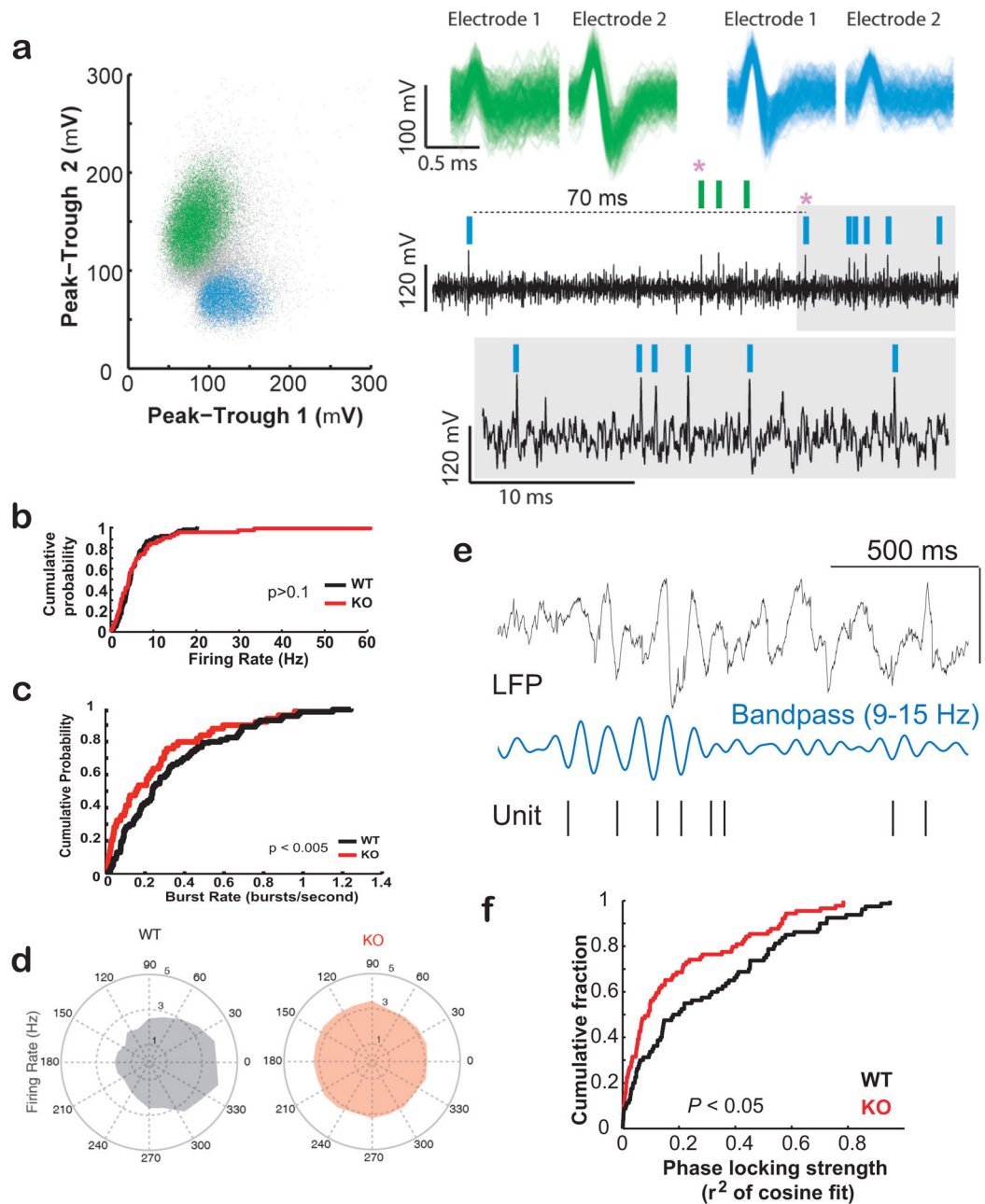


Extended Data Figure 1. Developmental expression pattern of *Ptchd1*
a–d, *In situ* hybridization labeling of *Ptchd1* mRNA at (a) P0 (coronal), (b) P15 (coronal), and (c–d) P35 (coronal and sagittal) from 3 C57/BL6 WT mice per age. White arrows indicate location of TRN region (scale bar = 1 mm).



Extended Data Figure 2. Generation of *Ptchd1* KO mouse

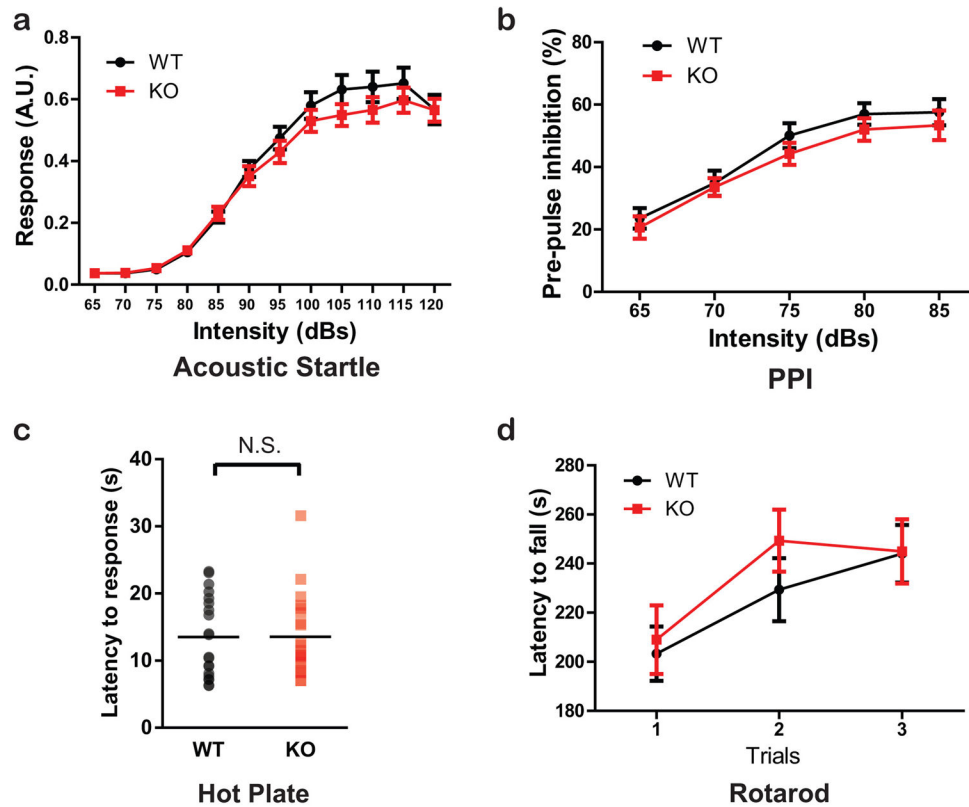
a, Diagram depicting the “full-length” and non-functional “Exons 1+3” *Ptchd1* isoforms. Genetic ablation of Exon 2 results in the removal of a majority of the transmembrane domains normally present in the endogenous full-length isoform. **b**, Schematic describing strategy to create *Ptchd1* KO mouse. Mice containing targeted allele were crossed to β -Actin Flp mice to remove the Neo cassette and β -Actin Cre mice to excise Exon 2. **c**, *In situ* hybridization probes targeting Exon 2 confirm successful genetic ablation of full-length *Ptchd1* mRNA (scale bar = 1 mm). **d**, PCR genotyping confirms deletion of Exon 2 from genome of male KO mice. **e**, qPCR of WT and KO cDNA samples shows removal of full-length *Ptchd1* isoform.



Extended Data Figure 3. Burst and spindle phase locking characteristics of *Ptcld1* KO and WT TRN neurons *in vivo*

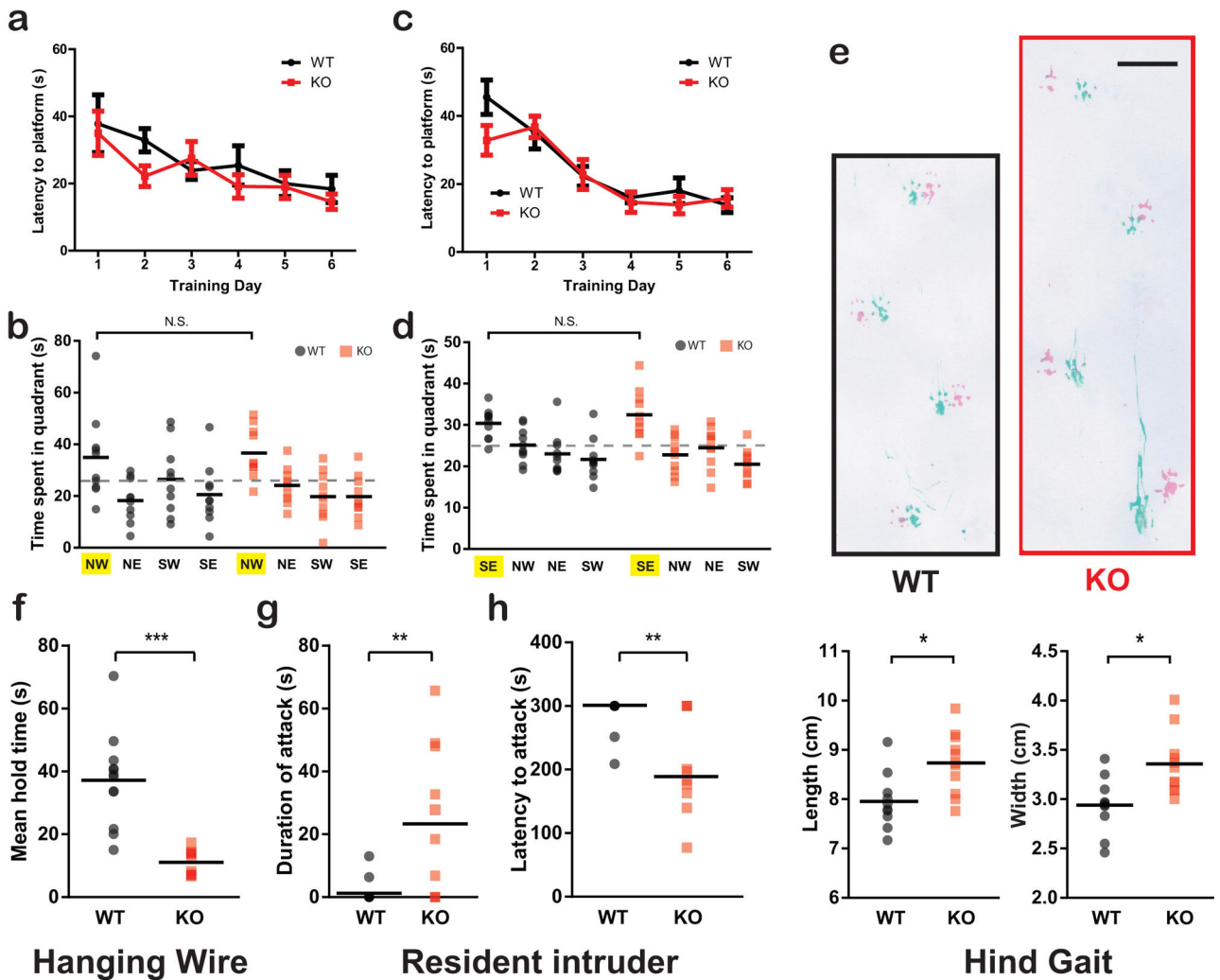
a, left, Example of unit clustering for a stereotrode recording. Two units (green and blue) are clearly separated when plotting peak-trough of the two electrodes of the stereotrode against each other. **right**, Spike-wave form of the two clustered units as they appear on the two electrodes of the stereotrode. Raw trace below shows a burst discharge (asterisk) of each unit during NREM sleep with colored ticks indicating corresponding individual spikes. A burst was identified as at least 2 spikes with an ISI ≤ 10 ms preceded by a period of 70 ms silence. Enlarged trace shows the accelerando-decelerando firing pattern characteristic for a TRN burst. **b**, Firing rate during NREM sleep is comparable between genotypes (89 WT, 80 KO

cells from 4 WT, 3 KO mice; $P > 0.1$ Kolmogorov-Smirnov statistics). **c**, *Ptchd1* KO TRN neurons show reduced propensity to generate bursts, even when excluding the 10% of KO cells with the highest firing rate (89 WT, 72 KO cells from 4 WT, 3 KO mice; $P < 0.05$ Kolmogorov-Smirnov statistics). **d**, Spindle-phase histogram for an example WT and KO neuron. Note that the WT neuron shows a preferred phase around the peak (0 degrees) of the spindle oscillation in WT but not KO. **e**, Example LFP recording (top) showing the temporal alignment of TRN spikes (bottom) to the preferred phase of the spindle activity (9–15 Hz, middle). **f**, *Ptchd1* KO mice show reduced phase-locking strength to spindle activity compared to WT littermates (89 WT, 80 KO cells from 4 WT, 3 KO mice).



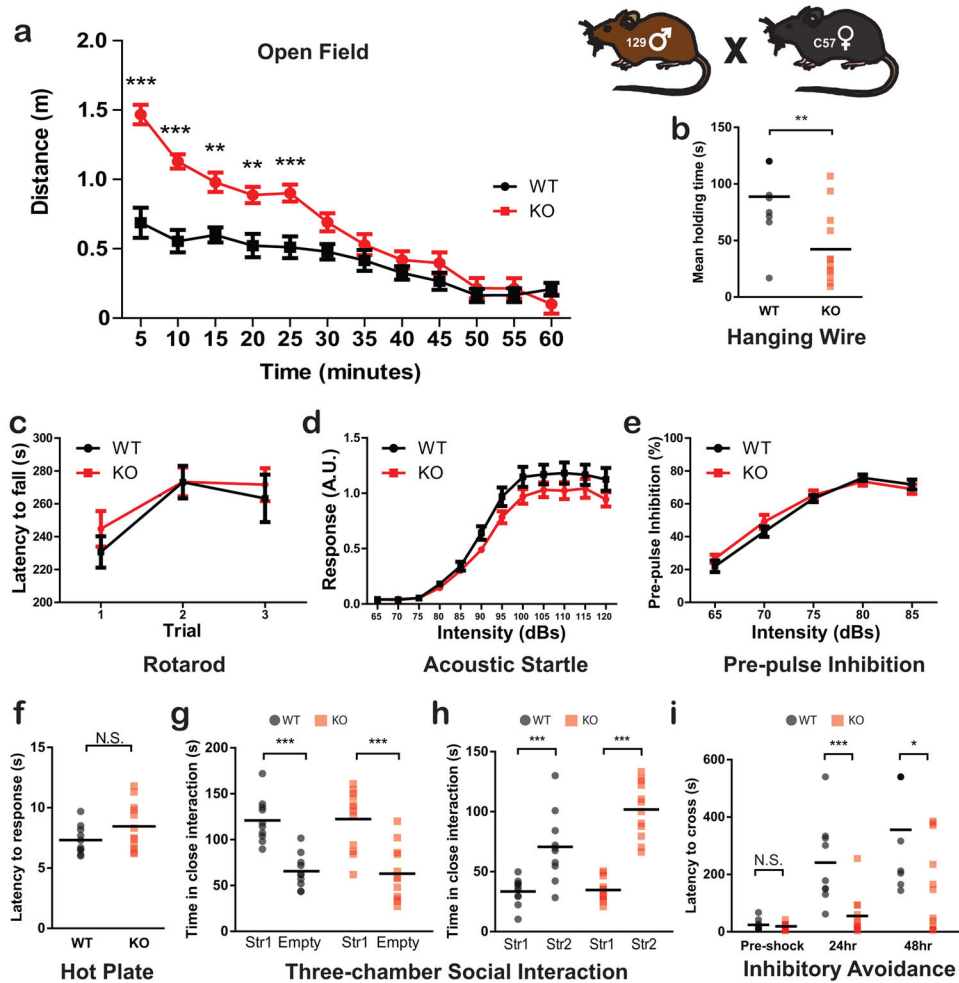
Extended Data Figure 4. *Ptchd1* KO mice have intact sensory responses and rotarod performance

a–c, Normal (a) acoustic startle (20 WT, 20 KO), (b) pre-pulse inhibition (20 WT, 20 KO) and (c) hot plate response in *Ptchd1* KO mice (20 WT, 21 KO). **d**, *Ptchd1* KO mice show normal motor coordination on the accelerating rotarod test (19 WT, 20 KO). Two-tailed t-tests (c) and two-way repeated measures ANOVA with Bonferroni post-hoc tests (a–b, d) were used for statistical analysis. Mean \pm s.e.m. N.S. = not significant.



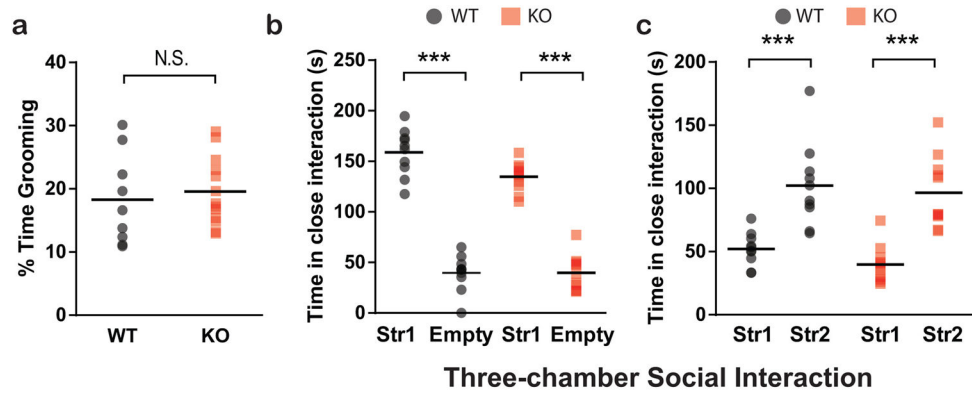
Extended Data Figure 5. Intact spatial learning but motor and aggression abnormalities in *Ptchd1* KO mice

a, Comparable learning curves between WT and KO mice during cued training protocol. **b**, Intact spatial learning demonstrated in 24hr probe trial. **c**, *Ptchd1* KO mice show normal reversal learning curve. **d**, No significant difference between WT and KO mice in 24 hour probe trial after reversal learning protocol (10 WT, 10 KO). **e**, Representative images of WT (black) and KO (red) strides. Forepaw position is represented by green paint and hindpaw position is represented by pink paint (scale bar = 2cm). Quantification reveals elongated stride length and width (10 WT, 11 KO). **f**, KO mice show drastic reductions in grip strength as measured by the hanging wire test (12 WT, 11 KO). **g-h**, KO mice attack intruder mice for a longer duration (**g**) and with a shorter latency to attack (**h**) in the resident-intruder test for aggression (10 WT, 10 KO). Two-way repeated measures ANOVA with Bonferroni post-hoc tests (**a**, **c**), one-way ANOVA with Bonferroni multiple comparison tests (**b**, **d**), two-tailed t-tests (**e**, **f**) and Wilcoxon ranksum tests (**g**, **h**) were used for statistical analysis. Mean \pm s.e.m. (**a**, **e**), mean (**b**, **d**, **e-f**), median (**g-h**). * $P < 0.05$; ** $P < 0.01$; *** $P < 0.001$; N.S. = not significant.

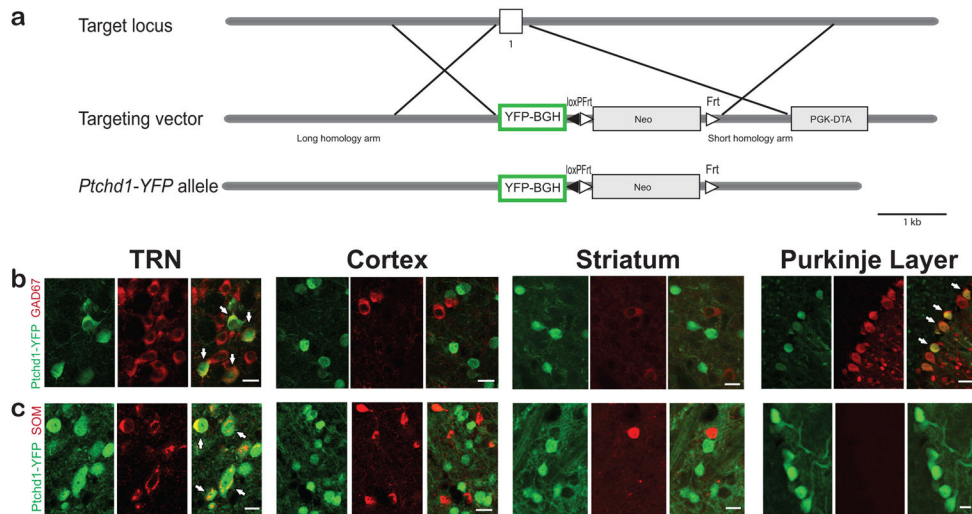


Extended Data Figure 6. Hyperactivity, hypotonia, and learning deficits in C57/129 *Ptchd1* KO mice

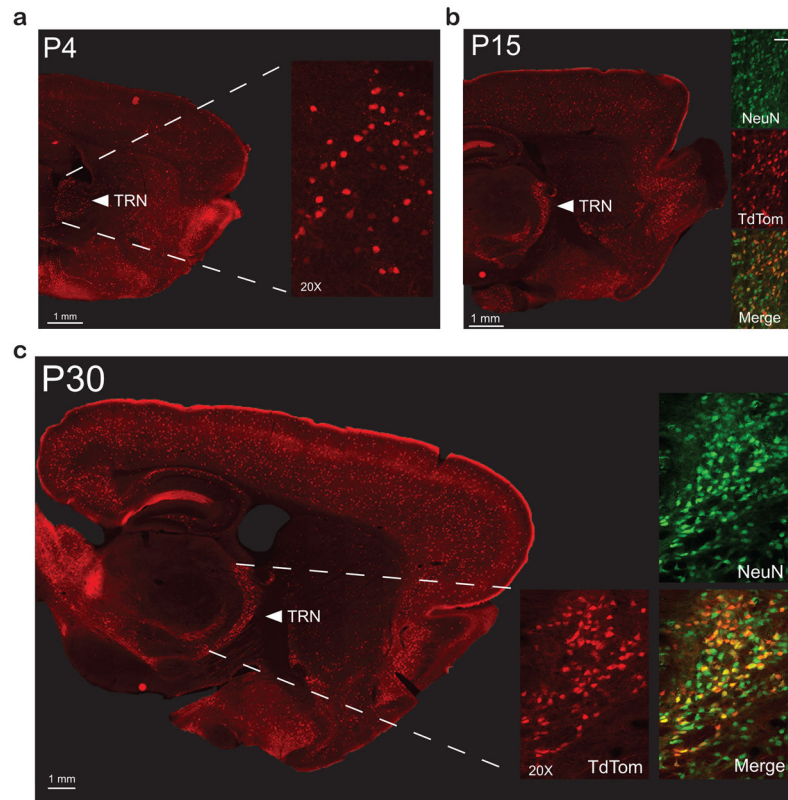
a, *Ptchd1* KO mice showed increased locomotor activity (10 WT, 11 KO). **b**, KO mice show decreased mean holding time in the hanging wire test (10 WT, 12 KO) but **c**, normal motor coordination in the rotarod task (10 WT, 10 KO). **d–f**, Sensory responses as measured by acoustic startle (**d**), pre-pulse inhibition (**e**), and hot plate (**f**) are also normal in KO mice (10 WT, 12 KO). **g–h**, Normal sociability (**g**) and novel social recognition (**h**) in mixed background *Ptchd1* KO mice (10 WT, 11 KO). **i**, KO mice show impaired associative learning and memory in the inhibitory avoidance task (9 WT, 12 KO). Two-tailed t-tests (**b**, **f**), one-way ANOVA with Bonferroni multiple comparison tests (**g–h**), and two-way repeated measures ANOVA with Bonferroni post-hoc tests (**a**, **c–e**, **i**) were used for statistical analysis. Mean \pm s.e.m. *P<0.05; **P<0.01; ***P<0.001; N.S. = not significant.



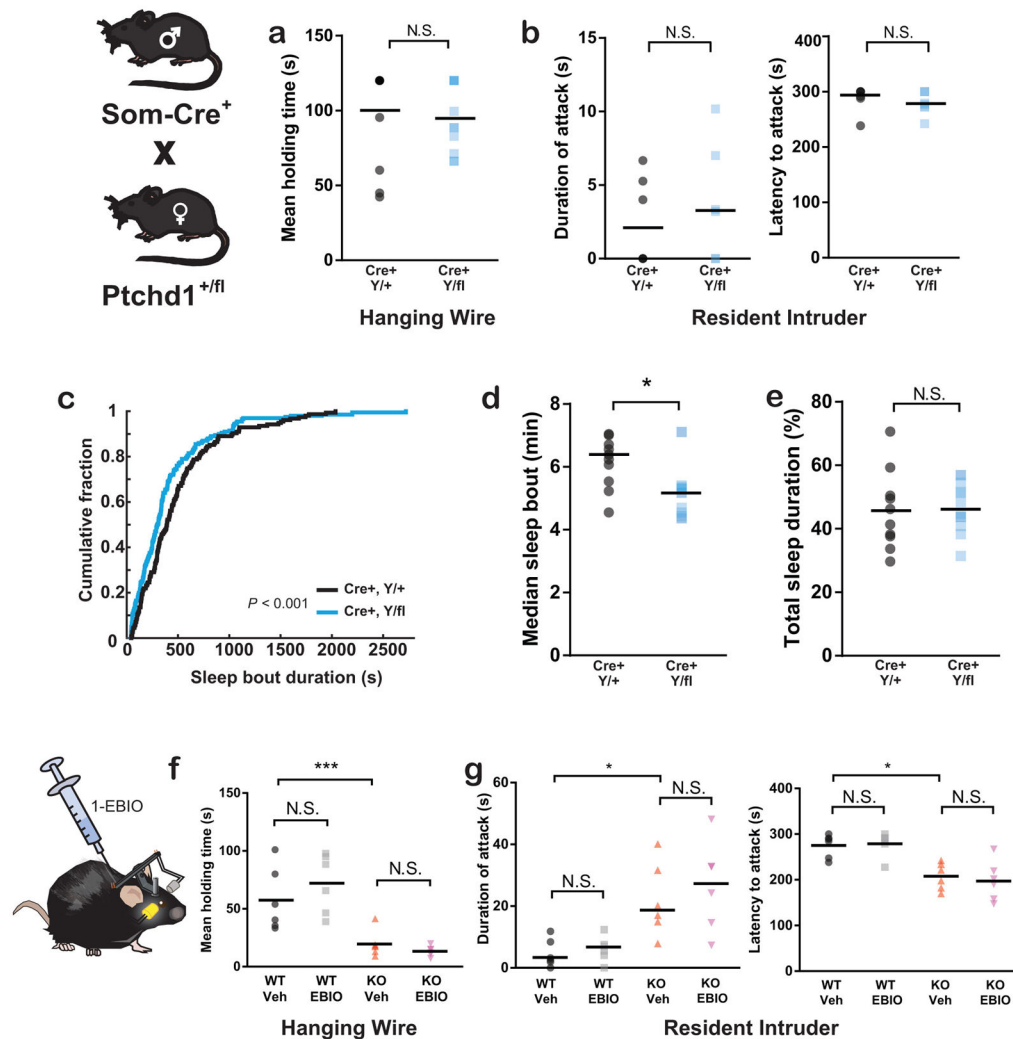
Extended Data Figure 7. Normal grooming and social interaction behaviors in *Ptchd1* KO mice
a, KO mice do not show excessive or injurious grooming behaviors (9 WT, 13 KO). **b–c**, KO mice (**b**) spent comparable amounts of time interacting with stranger mice in the three-chambered social interaction task and (**c**) display normal social novelty behaviors (10 WT, 11 KO). Two-tailed t-tests (**a**) and two-way repeated measures ANOVA with Bonferroni post-hoc tests (**b–c**) were used for statistical analysis. Bar in scatterplot denotes mean. *** $P < 0.001$; N.S. = not significant.



Extended Data Figure 8. YFP overlap with SOM interneuron marker is primarily confined to the TRN in *Ptchd1*-YFP mice
a, Schematic describing strategy to create *Ptchd1*-YFP mouse in which Exon 1 was replaced with YFP cassette. **b**, YFP-positive cells co-label with GAD67 antibody in TRN and the Purkinje layer of the cerebellum, but not in cortex or striatum. **c**, YFP-positive cells also co-label with SOM antibody in TRN, but not in other structures. Arrows denote overlap. (bar = 20 μ m).



Extended Data Figure 9. *Som-Cre* recombinase activity is early and robust in TRN neurons
a, P4 *Som-Cre⁺:TdTomato⁺* brains show TdTomato⁺ cells in the TRN. Inset shows magnified image taken with 20X objective. **b–c**, At (b) P15 and (c) P30, Cre recombinase activity in the TRN of the *Som-Cre⁺:TdTomato⁺* brains is robust, as shown by the inset depicting the significant TdTomato overlap with the pan-neuronal marker NeuN.



Extended Data Figure 10. Genetic disruption of *Ptchd1* TRN expression affects sleep stability but not grip strength or aggressive behaviors

a–b, *Som-Cre⁺:Ptchd1^{Y/fI}* mice appear normal in (a) the hanging wire (12 *Ptchd1^{Y/+}*, 11 *Ptchd1^{Y/fI}*) and (b) resident intruder task (6 *Ptchd1^{Y/+}*, 6 *Ptchd1^{Y/fI}*). **c–e**, *Som-Cre⁺:Ptchd1^{Y/fI}* mice show reductions in sleep bout duration as shown in (c) cumulative probability plot and (d) comparison of medians with (e) no differences in total time spent sleeping when compared to *Som-Cre⁺:Ptchd1^{Y/+}* littermates (10 *Ptchd1^{Y/+}*, 10 *Ptchd1^{Y/fI}*). **f–g**, 1-EBIO treatment has no effect on performance on (f) the hanging wire or (g) resident intruder task (6 WT-Veh, 6 WT-EBIO, 6 KO-Veh, 6 KO-EBIO). Kolomgorov-Smirnov test (a), Wilcoxon ranksum tests (b–c), two-tailed t-tests (d), and two-way repeated measures ANOVA with Bonferroni post-hoc tests (f), and Kruskal-Wallis with Dunn’s multiple comparisons tests were used for statistical analysis. Median (b–c, e–g), mean (d,f). *P<0.05; **P<0.01; ***P<0.001; N.S. = not significant.

Supplementary Material

Refer to Web version on PubMed Central for supplementary material.

Acknowledgments

We thank Ruqi Tang for insightful discussion during the initiation of the project, Huaiying Wang, Triana Dalia, Elaine Kwan, Heather Zaniewski for technical support, and Dr. John Vincent (Centre for Addiction and Mental Health, Toronto, Canada) for insightful discussion. We thank Dr. Jeremy Petravicz and Travis Emery from the Sur lab (MIT) for assistance with Ca^{2+} imaging and Dr. Arnold Heynen from the Bear lab (MIT) for technical advice on the inhibitory avoidance task. We thank all members of the Feng lab for their help and support. We thank Mick and Joshua Ball (Newcastle, Australia) for their insight and inspiration throughout this project. This work was supported by a grant from Simons Foundation Autism Research Initiative (SFARI Award ID: 307913) to GF and MMH, NIH grants to GF (NIH/NIMH, R01MH097104) and MMH (R01MH107680), and funds from the Poitras Center for Affective Disorders Research and the Stanley Center for Psychiatric Research at the Broad Institute of MIT and Harvard to GF. MFW is supported by an NIH Ruth L. Kirschstein National Research Service Award (FMH098641A). RDW is supported by the Swiss National Science Foundation.

References

1. Coe BP, Girirajan S, Eichler EE. The genetic variability and commonality of neurodevelopmental disease. *Am J Med Genet C Semin Med Genet.* 2012; 160C(2):118–29. [PubMed: 22499536]
2. Coe BP, Girirajan S, Eichler EE. A genetic model for neurodevelopmental disease. *Curr Opin Neurobiol.* 2012; 22(5):829–36. [PubMed: 22560351]
3. Zhou Y, et al. Mice with Shank3 Mutations Associated with ASD and Schizophrenia Display Both Shared and Distinct Defects. *Neuron.* 2016; 89(1):147–62. [PubMed: 26687841]
4. Cristino AS, et al. Neurodevelopmental and neuropsychiatric disorders represent an interconnected molecular system. *Mol Psychiatry.* 2014; 19(3):294–301. [PubMed: 23439483]
5. Noor A, et al. Disruption at the PTCHD1 Locus on Xp22.11 in Autism spectrum disorder and intellectual disability. *Sci Transl Med.* 2010; 2(49):49ra68.
6. Pinto D, et al. Functional impact of global rare copy number variation in autism spectrum disorders. *Nature.* 2010; 466(7304):368–72. [PubMed: 20531469]
7. Whibley AC, et al. Fine-scale survey of X chromosome copy number variants and indels underlying intellectual disability. *Am J Hum Genet.* 2010; 87(2):173–88. [PubMed: 20655035]
8. Marshall CR, et al. Structural variation of chromosomes in autism spectrum disorder. *Am J Hum Genet.* 2008; 82(2):477–88. [PubMed: 18252227]
9. Filges I, et al. Deletion in Xp22.11: PTCHD1 is a candidate gene for X-linked intellectual disability with or without autism. *Clin Genet.* 2011; 79(1):79–85. [PubMed: 21091464]
10. Torricco B, et al. Contribution of common and rare variants of the PTCHD1 gene to autism spectrum disorders and intellectual disability. *Eur J Hum Genet.* 2015; 23(12):1694–701. [PubMed: 25782667]
11. Chaudhry A, et al. Phenotypic spectrum associated with PTCHD1 deletions and truncating mutations includes intellectual disability and autism spectrum disorder. *Clin Genet.* 2015; 88(3):224–33. [PubMed: 25131214]
12. Halassa MM, et al. State-dependent architecture of thalamic reticular subnetworks. *Cell.* 2014; 158(4):808–21. [PubMed: 25126786]
13. Wimmer RD, et al. Thalamic control of sensory selection in divided attention. *Nature.* 2015; 526(7575):705–9. [PubMed: 26503050]
14. Pinault D. The thalamic reticular nucleus: structure, function and concept. *Brain Res Brain Res Rev.* 2004; 46(1):1–31. [PubMed: 15297152]
15. Guillery RW, Feig SL, Lozsadi DA. Paying attention to the thalamic reticular nucleus. *Trends Neurosci.* 1998; 21(1):28–32. [PubMed: 9464683]
16. Halassa MM, et al. Selective optical drive of thalamic reticular nucleus generates thalamic bursts and cortical spindles. *Nat Neurosci.* 2011; 14(9):1118–20. [PubMed: 21785436]
17. Bartho P, et al. Ongoing network state controls the length of sleep spindles via inhibitory activity. *Neuron.* 2014; 82(6):1367–79. [PubMed: 24945776]
18. von Krosigk M, Bal T, McCormick DA. Cellular mechanisms of a synchronized oscillation in the thalamus. *Science.* 1993; 261(5119):361–4. [PubMed: 8392750]

19. Marlinski V, Sirota MG, Beloozerova IN. Differential gating of thalamocortical signals by reticular nucleus of thalamus during locomotion. *J Neurosci*. 2012; 32(45):15823–36. [PubMed: 23136421]
20. Eerlij D, et al. Dopamine D4 receptor stimulation in GABAergic projections of the globus pallidus to the reticular thalamic nucleus and the substantia nigra reticulata of the rat decreases locomotor activity. *Neuropharmacology*. 2012; 62(2):1111–8. [PubMed: 22108379]
21. McAlonan K, Cavanaugh J, Wurtz RH. Guarding the gateway to cortex with attention in visual thalamus. *Nature*. 2008; 456(7220):391–4. [PubMed: 18849967]
22. Zhong Y, et al. Comprehensive analysis of patched domain-containing genes reveals a unique evolutionary pattern. *Genet Mol Res*. 2014; 13(3):7318–31. [PubMed: 24615097]
23. Goodrich LV, et al. Altered neural cell fates and medulloblastoma in mouse patched mutants. *Science*. 1997; 277(5329):1109–13. [PubMed: 9262482]
24. Rohatgi R, Milenkovic L, Scott MP. Patched1 regulates hedgehog signaling at the primary cilium. *Science*. 2007; 317(5836):372–6. [PubMed: 17641202]
25. Jasper H. Diffuse projection systems: the integrative action of the thalamic reticular system. *Electroencephalogr Clin Neurophysiol*. 1949; 1(4):405–19. discussion 419–20. [PubMed: 18421831]
26. Cueni L, et al. T-type Ca²⁺ channels, SK2 channels and SERCAs gate sleep-related oscillations in thalamic dendrites. *Nat Neurosci*. 2008; 11(6):683–92. [PubMed: 18488023]
27. Jahnsen H, Llinas R. Voltage-dependent burst-to-tonic switching of thalamic cell activity: an in vitro study. *Arch Ital Biol*. 1984; 122(1):73–82. [PubMed: 6087765]
28. Astori S, et al. The Ca(V)3.3 calcium channel is the major sleep spindle pacemaker in thalamus. *Proc Natl Acad Sci U S A*. 2011; 108(33):13823–8. [PubMed: 21808016]
29. Huguenard JR, Prince DA. A novel T-type current underlies prolonged Ca(2+)-dependent burst firing in GABAergic neurons of rat thalamic reticular nucleus. *J Neurosci*. 1992; 12(10):3804–17. [PubMed: 1403085]
30. Ying SW, Goldstein PA. Propofol-block of SK channels in reticular thalamic neurons enhances GABAergic inhibition in relay neurons. *J Neurophysiol*. 2005; 93(4):1935–48. [PubMed: 15563549]
31. Coulon P, et al. Burst discharges in neurons of the thalamic reticular nucleus are shaped by calcium-induced calcium release. *Cell Calcium*. 2009; 46(5–6):333–46. [PubMed: 19913909]
32. Brunetti PM, et al. Design and fabrication of ultralight weight, adjustable multi-electrode probes for electrophysiological recordings in mice. *J Vis Exp*. 2014; (91):e51675. [PubMed: 25225749]
33. Ferrarelli F, et al. Reduced sleep spindle activity in schizophrenia patients. *Am J Psychiatry*. 2007; 164(3):483–92. [PubMed: 17329474]
34. Limoges E, et al. Atypical sleep architecture and the autism phenotype. *Brain*. 2005; 128(Pt 5): 1049–61. [PubMed: 15705609]
35. Dang-Vu TT, et al. Spontaneous brain rhythms predict sleep stability in the face of noise. *Current Biology*. 2010; 20(15):R626–R627. [PubMed: 20692606]
36. Wimmer RD, et al. Sustaining Sleep Spindles through Enhanced SK2-Channel Activity Consolidates Sleep and Elevates Arousal Threshold. *Journal of Neuroscience*. 2012; 32(40): 13917–13928. [PubMed: 23035101]
37. Grimley JS, et al. Visualization of synaptic inhibition with an optogenetic sensor developed by cell-free protein engineering automation. *J Neurosci*. 2013; 33(41):16297–309. [PubMed: 24107961]
38. Remington A, et al. Selective attention and perceptual load in autism spectrum disorder. *Psychol Sci*. 2009; 20(11):1388–93. [PubMed: 19843262]
39. Sachs GS, et al. Comorbidity of attention deficit hyperactivity disorder with early- and late-onset bipolar disorder. *Am J Psychiatry*. 2000; 157(3):466–8. [PubMed: 10698829]
40. Leyfer OT, et al. Comorbid psychiatric disorders in children with autism: interview development and rates of disorders. *J Autism Dev Disord*. 2006; 36(7):849–61. [PubMed: 16845581]
41. Won H, et al. GIT1 is associated with ADHD in humans and ADHD-like behaviors in mice. *Nat Med*. 2011; 17(5):566–72. [PubMed: 21499268]
42. Spencer T, et al. Efficacy of a mixed amphetamine salts compound in adults with attention-deficit/hyperactivity disorder. *Arch Gen Psychiatry*. 2001; 58(8):775–82. [PubMed: 11483144]

43. Curzon, P.; Rustay, NR.; Browman, KE. Cued and Contextual Fear Conditioning for Rodents. In: Buccafusco, JJ., editor. *Methods of Behavior Analysis in Neuroscience*. Boca Raton (FL): 2009.
44. Nestler EJ, Hyman SE. Animal models of neuropsychiatric disorders. *Nat Neurosci*. 2010; 13(10): 1161–9. [PubMed: 20877280]
45. Meyer AH, et al. In vivo labeling of parvalbumin-positive interneurons and analysis of electrical coupling in identified neurons. *J Neurosci*. 2002; 22(16):7055–64. [PubMed: 12177202]
46. Graybiel AM, Elde RP. Somatostatin-like immunoreactivity characterizes neurons of the nucleus reticularis thalami in the cat and monkey. *J Neurosci*. 1983; 3(6):1308–21. [PubMed: 6133921]
47. Taniguchi H, et al. A resource of Cre driver lines for genetic targeting of GABAergic neurons in cerebral cortex. *Neuron*. 2011; 71(6):995–1013. [PubMed: 21943598]
48. Chen Z, et al. Thalamic circuit mechanisms link sensory processing in sleep and attention. *Frontiers in Neural Circuits*. 2015
49. Zikopoulos B, Barbas H. Pathways for emotions and attention converge on the thalamic reticular nucleus in primates. *J Neurosci*. 2012; 32(15):5338–50. [PubMed: 22496579]
50. Fisher SP, et al. Rapid assessment of sleep-wake behavior in mice. *J Biol Rhythms*. 2012; 27(1): 48–58. [PubMed: 22306973]

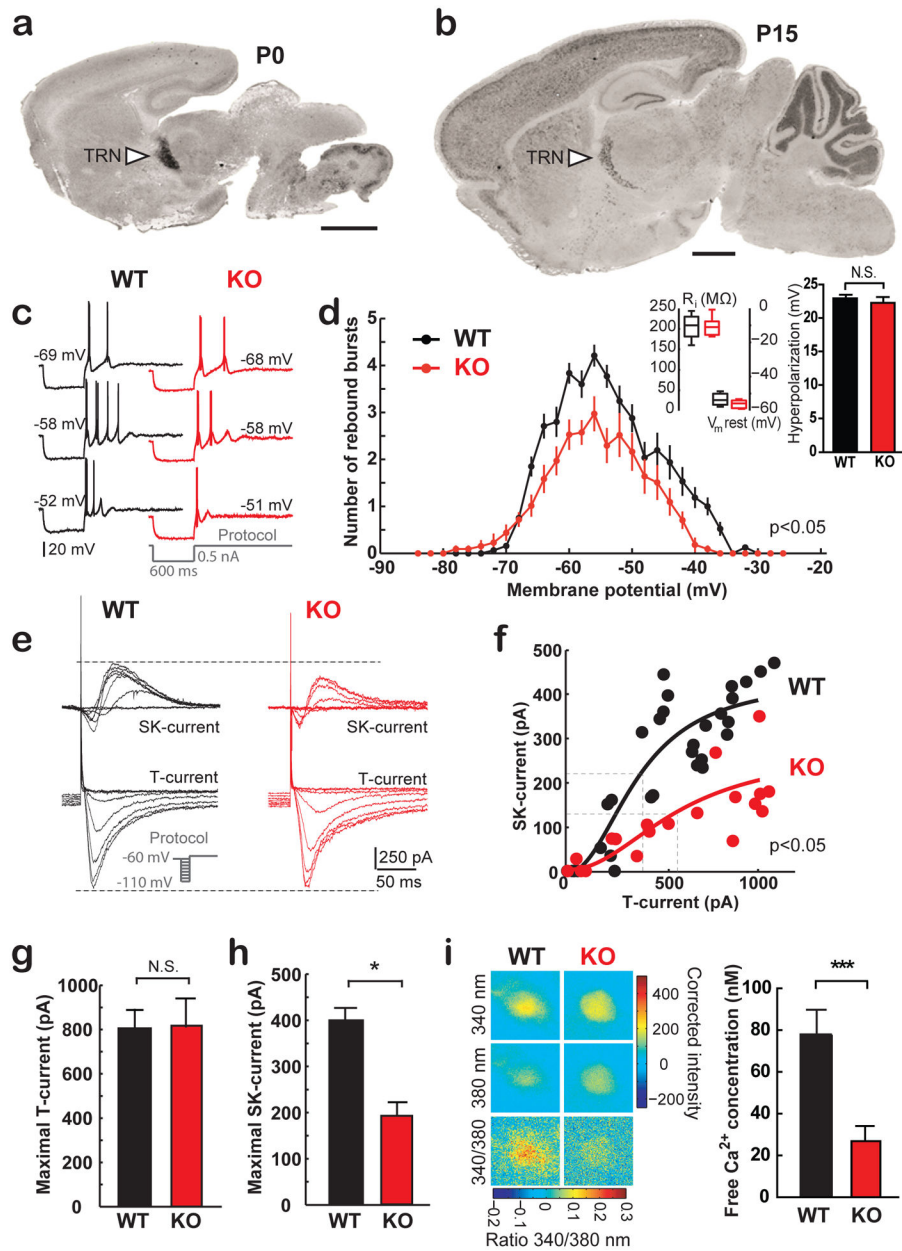


Figure 1. Impaired repetitive bursting and SK2 currents in KO TRN neurons
a–b, *Ptchd1* expression (3 WT mice). Bar = 1 mm. **c**, Representative TRN burst traces (out of 8 WT, 9 KO cells). **d**, Reduced burst firing in KO TRN neurons (8 WT, 9 KO cells). **e**, Representative T and SK2 current traces. **f**, Normal T (g) and reduced SK2 currents (h) in KO cells (8 WT, 9 KO). **i**, Diminished free $[Ca^{2+}]_i$ in KO cells. Representative heat maps show background-corrected intensity (37 WT, 36 KO cells). Wilcoxon ranksum (d, f–h) and two-tailed t-tests (i). Mean \pm s.e.m. * $P < 0.05$; *** $P < 0.001$; N.S.=not significant.

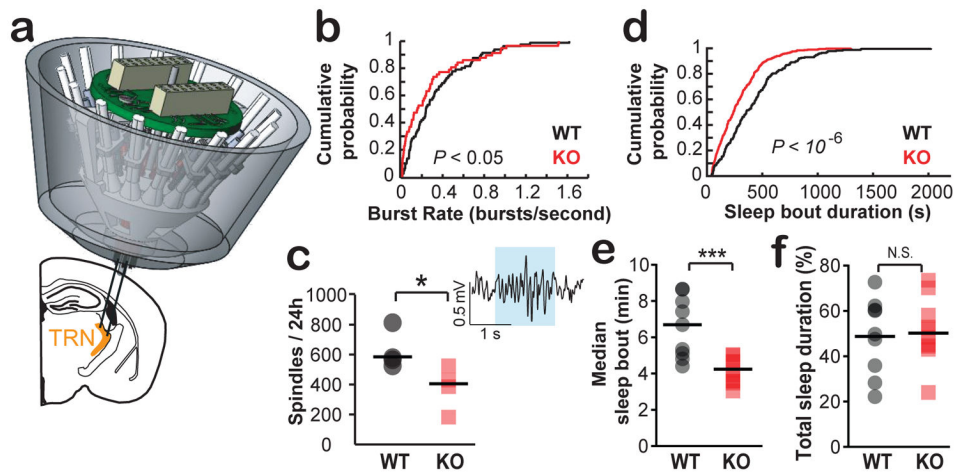


Figure 2. Decreased spindles and sleep fragmentation in KO mice

a, Multi-electrode implant targeting TRN **b**, Decreased TRN burst discharge in KOs (89 WT, 80 KO cells from 4 WT, 3 KO mice). **c**, Reduced spindles in KOs. **d–f**, KOs display shorter sleep bouts with normal total sleep duration (9 WT, 10 KO). Kolomgorov-Smirnov (b, d) and Wilcoxon ranksum tests (c, e–f). Median (c, e–f). * $P < 0.05$; *** $P < 0.001$; N.S.=not significant.

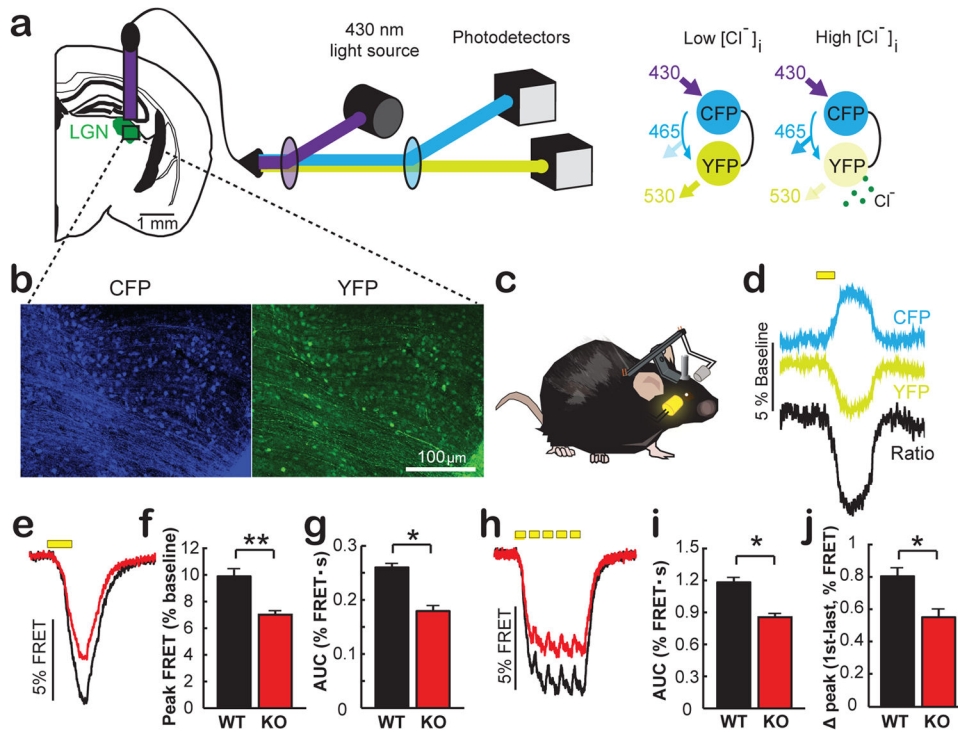


Figure 3. Reduced sensory-evoked thalamic inhibition in KO mice

a, Schematic of CFP-to-YFP FRET. **b**, Confocal images of superclomeleon expression in LGN (bar = 100 μ m). **c**, Stimuli delivered to the eye contra-lateral to implanted LGN. **d**, Example traces of visually-evoked CFP and YFP fluorescence changes. **e–g**, Reduced LGN inhibition in KOs reflected in peak FRET response (**f**) and smaller area under the curve (**g**; AUC) (6 WT, 6 KO mice). **h–j**, KOs also show decreased facilitation of FRET response (6 WT, 6 KO mice). Wilcoxon ranksum tests (**e–j**). Mean \pm s.e.m. *P < 0.05; **P < 0.01

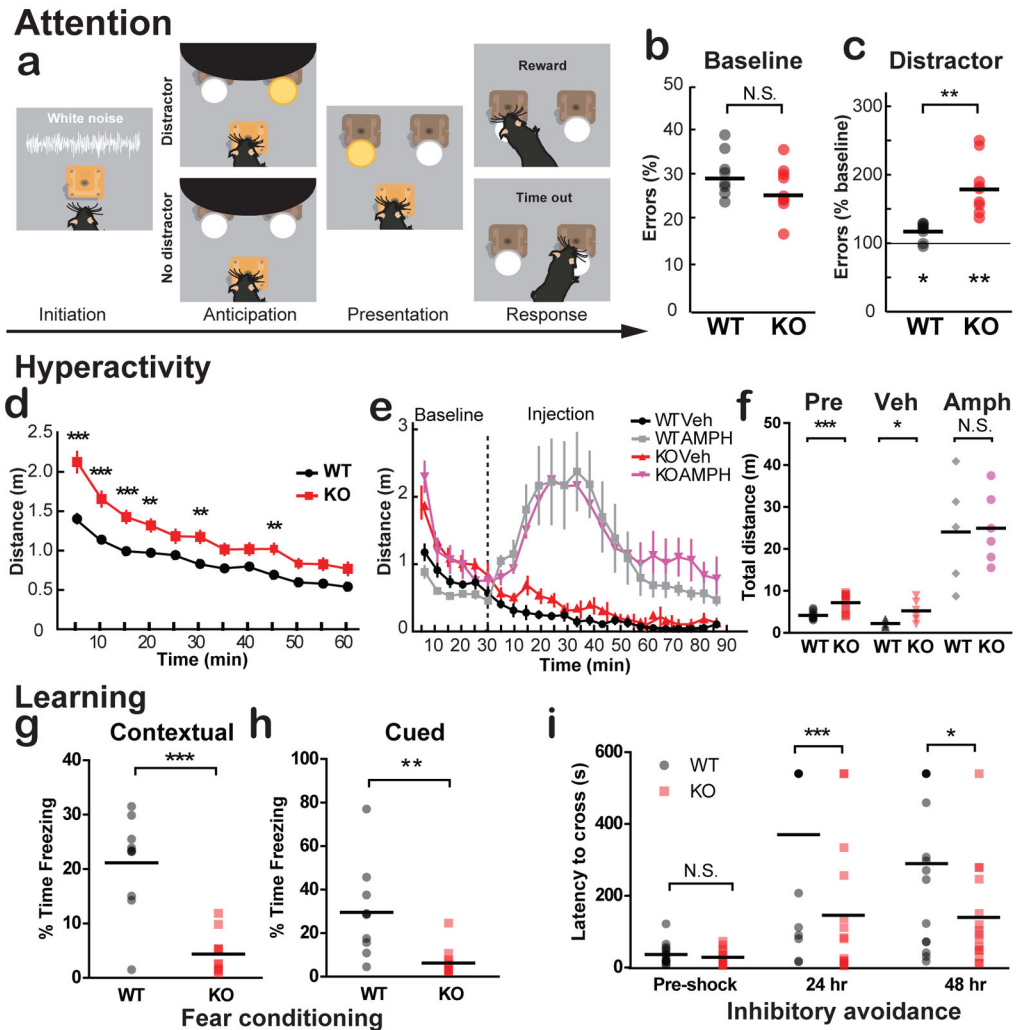


Figure 4. KO mice show attention, locomotor, and learning impairment

a, Visual detection task design (8 WT, 9 KO). **b**, KOs showed comparable baseline performance. **c**, KOs displayed decreased accuracy in the presence of distractors. **d**, KOs show increased locomotion in open field (30 WT, 31 KO). **e–f**, KOs show normal responses to amphetamine (5 WT-Veh, 6 WT-Amph, 5 KO-Veh, 6 KO-Amph). **g–h**, KOs exhibit decreased fear-induced learning behaviors in (g) contextual and (h) cued fear conditioning tests (10 WT, 11 KO). **i**, Diminished KO latency to cross in inhibitory avoidance task (24 WT, 23 KO). Wilcoxon ranksum (b–c), two-tailed t (g–h), and two-way RM ANOVA with Bonferroni post-hoc tests (d–f, i). * $P < 0.05$; ** $P < 0.01$; *** $P < 0.001$; N.S.=not significant.

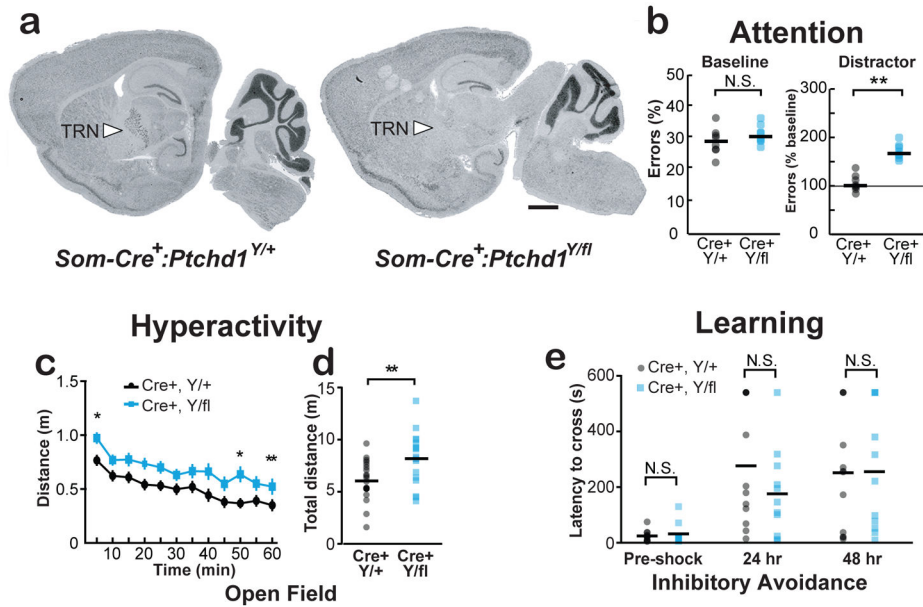


Figure 5. TRN dysfunction explains ADHD-like behaviors in KO

a, *Ptchd1* ablation from TRN (bar = 1 mm). **b**, *Som-Cre⁺:Ptchd1^{Y/fl}* mice recapitulate attention deficits observed in KOs (8 *Ptchd1^{Y/+}*, 8 *Ptchd1^{Y/fl}*). **c–d**, *Som-Cre⁺:Ptchd1^{Y/fl}* mice are hyperactive (21 *Ptchd1^{Y/+}*, 22 *Ptchd1^{Y/fl}*). **e**, *Som-Cre⁺:Ptchd1^{Y/fl}* mice show intact ability to form complex association (11 *Ptchd1^{Y/+}*, 12 *Ptchd1^{Y/fl}*). Wilcoxon ranksum (b), two-tailed t (d), and two-way RM ANOVA with Bonferroni post-hoc tests (c, e). Median (b), mean ± s.e.m (c), mean (de). *P<0.05; **P<0.01; N.S.=not significant.

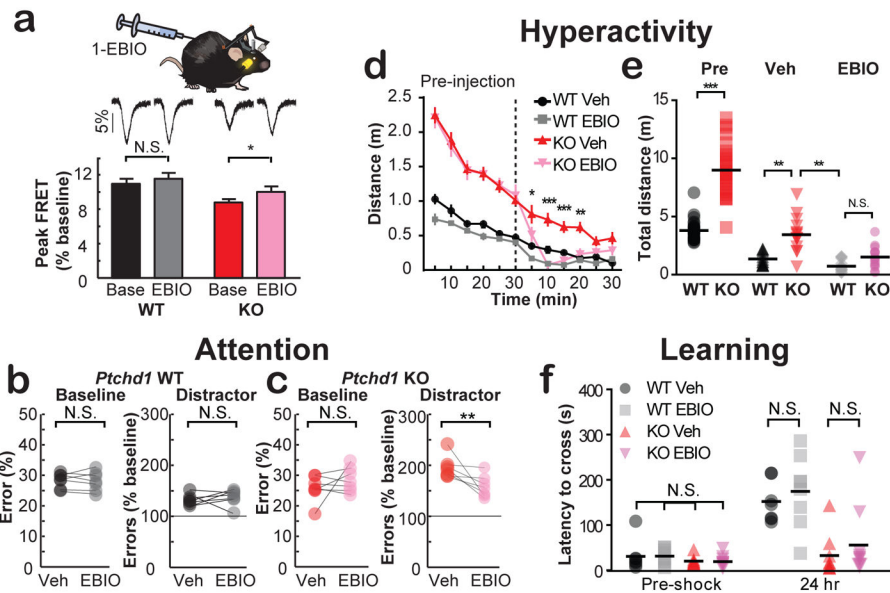


Figure 6. SK2 enhancement corrects ADHD-like KO symptoms

a, 1-EBIO corrects inhibitory transients in KOs (7 WT-Veh, 7 WT-EBIO, 7 KO-Veh, 7 KO-EBIO). **b–c**, 1-EBIO improves KO attention performance (7 WT-Veh, 7 WT-EBIO, 7 KO-Veh, 7 KO-EBIO). **d–e**, 1-EBIO rescues KO hyperactivity (13 WT-Veh, 13 WT-EBIO, 13 KO-Veh, 15 KO-EBIO). **f**, No 1-EBIO effects on inhibitory avoidance (7 WT-Veh, 8 WT-EBIO, 9 KO-Veh, 10 KO-EBIO). Wilcoxon ranksum (a–c) and two-way RM ANOVA with Bonferroni post-hoc tests (d–f). Mean \pm s.e.m. (a, d), mean (e–f) * $P < 0.05$; ** $P < 0.01$; *** $P < 0.001$; N.S. = not significant.